

AI Driven Laser Parameter Search: Inverse Design of Photonic Surfaces using Greedy Surrogate-based Optimization

Luka Grbic^{1*}, Minok Park², Juliane Müller³, Vassilia Zorba^{2,4},
Wibe Albert de Jong^{1*}

^{1*}Applied Mathematics and Computational Research, Lawrence Berkeley
National Laboratory, 1 Cyclotron Rd, Berkeley, 94720, California, USA.

²Energy Technologies Area, Lawrence Berkeley National Laboratory, 1
Cyclotron Rd, Berkeley, 94720, California, USA.

³Computational Science Center, National Renewable Energy Laboratory,
15013 Denver West Parkway, Golden, 80401, Colorado, USA.

⁴Department of Mechanical Engineering, University of California at
Berkeley, 6141 Etcheverry Hall, Berkeley, 94709, California, USA.

*Corresponding author(s). E-mail(s): lgrbcic@lbl.gov; wadejong@lbl.gov;
Contributing authors: minokpark@lbl.gov; juliane.mueller@nrel.gov;
vzorba@lbl.gov;

Abstract

Photonic surfaces designed with specific optical characteristics are becoming increasingly important for use in various energy harvesting and storage systems. In this study, we develop a surrogate-based optimization approach for designing such surfaces. The surrogate-based optimization framework employs the Random Forest algorithm and uses a greedy, prediction-based exploration strategy to identify the laser fabrication parameters that minimize the discrepancy relative to a user-defined target optical characteristics. We demonstrate the approach on two synthetic benchmarks and two specific cases of photonic surface inverse design targets. It exhibits superior performance when compared to other optimization algorithms across all benchmarks. Additionally, we demonstrate a technique of inverse design warm starting for changed target optical characteristics which enhances the performance of the introduced approach.

Keywords: inverse design, photonic surfaces, surrogate-based optimization, femtosecond laser processing, machine learning, random forests

1 Introduction

The photonic surface is a type of material that is excellent at absorbing light and emitting thermal radiation. Its efficiency depends on its spectral absorptivity and emissivity, more specifically, how well it emits energy across different wavelengths when at a stable temperature. These quantities measure the energy emitted at each wavelength compared to that of an ideal emitter (Brewster (1992), Howell et al. (2020)). Photonic surfaces are increasingly used for energy applications like harvesting and storage. They are used in Thermophotovoltaic (TPV) systems (Fan et al. (2020), LaPotin et al. (2022)), radiative cooling systems (Raman et al. (2014), Heo et al. (2020)), solar-based water desalination systems (Menon et al. (2020), Ni et al. (2016)), and concentrated solar power systems (Weinstein et al. (2015), He et al. (2020)). Designing photonic surfaces to meet specific target spectral emissivity values is therefore a key optimization and inverse design task.

Modern approaches used for photonic materials inverse design can be sorted into two main categories: (i) Deep Learning (DL) (Wiecha et al. (2021), Ma et al. (2021)), and (ii) Optimization-based methods (Mao et al. (2021), Wang et al. (2021)). DL-based approaches are increasingly used and they include architectures like Tandem Neural Networks (Xu et al. (2021), Park et al. (2024)), Generative Adversarial Networks (GAN) (Ma et al. (2022), Jiang and Fan (2020)), and Autoencoders (AE) (Wiecha et al. (2021), Kudyshev et al. (2020)). These techniques are popular since they handle unstructured data that are common for parametrization of photonic materials (Liu et al. (2020), Liu et al. (2021), Kudyshev et al. (2020)). DL methods are beneficial as they can be reused for inverse design, provided that the same design space is considered. However, these methods require large amounts of data to achieve sufficient accuracy and this “cost” also needs to be taken into account (Habibi et al. (2023)). Moreover, if the design space of the target value drastically changes compared to that of the training data, DL approaches can struggle to accurately extrapolate.

Optimization-based methods for photonic inverse design can be further divided into two distinct categories. The first category is photonic inverse design using the adjoint optimization method (Zhu et al. (2023), Gershnel et al. (2022), Hughes et al. (2018), Minkov et al. (2020), Lalau-Keraly et al. (2013), Wang et al. (2020)). The adjoint optimization method is a specific type of the gradient-based optimization method that is generally computationally more efficient for inverse design (Molesky et al. (2018)). The main drawback is in its larger implementation complexity, as well as its dependency on simulations, i.e., it is not suitable for inverse design based on experimental data (Ma et al. (2021)).

The other category of optimization-based approaches are hybrid machine learning (ML) and optimization methods. A forward ML model is trained, also known as a surrogate model, that can quickly and efficiently predict a solution given on a design vector. The next step is to formulate the problem as an inverse design optimization problem that is solved by an optimization algorithm which employs the surrogate model to assess each design (Deng et al. (2022), Ma et al. (2021)). Another option is to use an ML surrogate to infer initial designs used for further simulation-optimization steps which has shown to be generally beneficial for inverse design tasks (Habibi et al. (2023)). Hybrid approaches include combinations like AE coupled with Differential

Evolution (DE) (Kudyshev et al. (2020)), fully connected DNNs with DE (Hegde (2019)), adjoint optimization with AEs (Kudyshev et al. (2020)), Long Short-term Memory networks with a gradient-free optimization algorithm (Yao et al. (2023)), adjoint optimization with GANs (Kudyshev et al. (2021)), Yeung et al. (2022)), adjoint optimization with Convolutional Neural Networks (Yeung et al. (2022)), and Random Forests (RF) with DE (Grbic et al. (2024)).

The overwhelming majority of previous literature are based on simulation data, and most have a unique design methodology tailored for a specific photonic material type and target property. Furthermore, design parameters often include complex topological information (Liu et al. (2020), Liu et al. (2021), Kudyshev et al. (2020)), Kudyshev et al. (2020)). Finally, previous research of photonic materials inverse design is mostly not focused on minimizing the required resources needed to train highly accurate ML models, nor the minimization of inverse design (simulation or experimental) function evaluations with optimization algorithms. This is an increasingly important aspect of inverse design that needs to be considered, especially in the era of self-driving laboratories and autonomous experimentation (Noack and Ushizima (2023), Häse et al. (2019)).

The inverse design approach we introduce here builds upon our previous work (Park et al. (2024), Grbic et al. (2024)) where we showed that it is possible to design photonic surfaces utilizing pulsed femtosecond laser ablation on surfaces of plain materials. We determine an inverse design mapping between laser fabrication parameters such as laser power, scanning speed, and spacing between consecutive scan lines, thereby bypassing the complex light-matter interaction physics, and complex topological data usually used for photonic inverse design. Furthermore, unlike the majority of previous inverse design methods, we utilize real experimental data originally presented in our previous work. The experimental data contains laser fabrication parameters and spectral emissivity curves for two different materials, namely stainless steel and Inconel.

Given all these major benefits over other approaches, we introduce the AI Laser Parameter Search (ALPS) optimization framework used for efficient inverse design of photonic surfaces. ALPS is a surrogate-based optimization approach that utilizes the RF algorithm and a prediction-based exploration strategy (Kochenderfer and Wheeler (2019)) to approximate a target design. This approach relies on evaluating the RF surrogate at specific designs, and then determining the optimal design or a batch of optimal designs for experimental model evaluation based on its distance or discrepancy relative to the target design. This simple greedy sampling strategy is shown to work efficiently on a set of benchmark problems (Paria et al. (2022), Wang et al. (2014)). The RF algorithm is used as it is shown to perform accurately and efficiently as a forward model for photonic surfaces in previous work (Grbic et al. (2024), Elzouka et al. (2020)).

Furthermore, one of the major benefits of ALPS is that the RF algorithm is trained to model the forward relationship of the photonic surface design (laser fabrication parameters and spectral emissivity) during the optimization process, and not the relationship between the input designs and their discrepancy relative to the target which is usually the case for most model-based optimization algorithms for inverse design.

This feature of ALPS implies re-usability through warm starting when the inverse design target is changed. It should be noted that this could also be achieved through Bayesian Optimization (BO) methods that utilize Gaussian Processes (GP) as they are extremely efficient, however, they require more complex implementations (Liu et al. (2018)) if we want to accurately capture the multi-input and multi-output relationships present in the photonic surface design, whereas in ALPS we can simply utilize an out-of-the-box RF algorithm.

Finally, in order to showcase the benefits of using ALPS for general and photonic surfaces inverse design optimization, we compare it with an array of other established optimization algorithms (including BO) on two synthetic benchmarks and four different photonic surfaces benchmark targets varied by both the used plain surface material (Stainless steel and Inconel) and the shape of the the target spectral emissivity curves. Furthermore, we show the re-usability of the ALPS approach for a cross-target and even cross-material inverse design process.

The remainder of this article is organized as follows. The photonic surface inverse design problem is introduced in Sec. 2. This section includes the formal mathematical definition of inverse design, the photonic surface design loop, the experimental models, the photonic surface design target benchmarks, and most importantly, the ALPS algorithm. The results of ALPS and other optimization algorithms for the synthetic and photonic inverse design benchmarks (with and without warm starting) are presented in Sec. 3. Details on the experimental data, machine learning experimental models and validation, synthetic benchmarks, algorithms used for comparison, and detailed results can be found in App. A, B, and C, respectively.

2 Photonic Surface Inverse Design

In this section, we introduce the mathematical definition of the general inverse design problem and notation, as well as the photonic surface inverse design problem. Furthermore, we define the photonic surface inverse design benchmarks and the algorithmic details of ALPS.

2.1 Mathematical Definition of Inverse Design

The objective of inverse design is to obtain a set of design parameters that yield a known target value or property. The inverse design problem is mathematically defined as:

$$\mathbf{x} = f^{-1}(\mathbf{y}) \quad (1)$$

In Eq. (1), $\mathbf{x} \in \mathbb{R}^M$ is the design vector, $\mathbf{y} \in \mathbb{R}^N$ is the target vector that is defined *a priori*, and $f : \mathbb{R}^M \rightarrow \mathbb{R}^N$ represents the objective function which in the case of inverse design is inverted, unlike in forward optimization problems. Inverse design problems are typically ill-posed, meaning that multiple values of \mathbf{x} can yield similar values of \mathbf{y} . As an optimization objective function, the inverse design problem is defined as:

$$\begin{aligned} & \underset{\mathbf{x}}{\text{minimize}} && \epsilon(f(\mathbf{x}), \mathbf{y}) \\ & \text{s. t.} && \mathbf{x}_{\text{lb}} \leq \mathbf{x} \leq \mathbf{x}_{\text{ub}} \end{aligned} \quad (2)$$

In Eq. (2), $\epsilon : \mathbb{R}^N \times \mathbb{R}^N \rightarrow \mathbb{R}$ is a measure of discrepancy between the desired target vector \mathbf{y} and the forward function f evaluated design vector \mathbf{x} . The design vector \mathbf{x} is defined as $\mathbf{x} = [x_1, \dots, x_M]^T$ in the decision space \mathbb{R}^M , where M is the dimension of vector. The objective here is to minimize ϵ , and ideally find a perfect match between $f(\mathbf{x})$ and \mathbf{y} , i.e., an ϵ value of 0. Moreover, during the minimization process, the design vector must be within predefined lower and upper boundaries, \mathbf{x}_{lb} and \mathbf{x}_{ub} , respectively.

For all inverse design benchmarks in this manuscript, the chosen discrepancy measure ϵ is equivalent to the Root Mean Square Error (RMSE), and mathematically, it is defined as:

$$\text{RMSE} = \sqrt{\frac{1}{N} \sum_{i=1}^N (y_i - f(\mathbf{x})_i)^2} \quad (3)$$

The variables y_i and $f(\mathbf{x})_i$ in Eq. (3) are the i^{th} components of the target vector \mathbf{y} and f evaluated at the design vector \mathbf{x} , respectively. The value of $f(\mathbf{x})$ is a vector itself and has the same number of components N as \mathbf{y} .

2.2 Photonic Surfaces Inverse Design Computational Framework

The relationship between laser fabrication parameters and spectral emissivity curves is utilized for the inverse design of photonic surfaces. The laser fabrication parameters are the laser power (W), scanning speed (mm/s), and spacing (μm), denoted as L_p , S_s , and S , respectively. The spectral emissivity curves are defined as N dimensional vectors ($N = 822$) where each component represents an emissivity value (0 to 1) for each of the N wavelength values (interval from 2.5 to 12.5 μm). Instead of inferring the spectral emissivity curves from the laser fabrication parameters experimentally, we use ML algorithms to accurately model this relationship (denoted as the experimental model throughout the manuscript). As shown in Fig. 1a, we utilize a combined RF and Principle Component Analysis (PCA) algorithms (denoted as RF-PCA) as it was shown in our previous work (Grbic et al. (2024)) that it is accurate and robust. Two experimental models are trained using two distinct datasets, differentiated by the type of plain surface materials used for texturing: Inconel (Grbic et al. (2024)) and Stainless Steel (Park et al. (2024)). Full details of the datasets, RF-PCA hyperparameters, and the experimental model validation procedure can be found in App. A.

Moreover, the photonic surface inverse design loop is shown in Fig. 1b. The principal aim of this loop is to determine the optimal laser fabrication parameters that yield a specific target spectral emissivity with the fewest possible evaluations of the experimental model. The process commences by generating an initial set of laser fabrication parameters through Latin Hypercube Sampling (LHS), followed by an update

of the ALPS framework. Secondly, the ALPS framework explores the laser fabrication parameter space and determines the design vector that should be evaluated by the experimental model to obtain the spectral emissivity value. The target and experimental model-inferred spectral emissivity curves are compared, and based on this discrepancy, the best laser parameters and corresponding spectral emissivity curves are selected to update the ALPS framework to improve its capacity for more precise parameter space exploration. The loop is terminated when the maximum number of experimental model evaluations is reached.

A visual example of the photonic surface inverse design process is shown in Fig. 1c. The goal is to minimize the discrepancy ϵ between the two curves as outlined in Eq. (2). The two spectral emissivity curves are the user-defined target spectral emissivity denoted as \mathbf{y} , and the spectral emissivity $f(\mathbf{x})$ generated by evaluating the design vector \mathbf{x} ($\mathbf{x} = [L_p, S_s, S]^T$) with the experimental model f . Due to differences in the material datasets, the lower and upper boundaries \mathbf{x}_{lb} and \mathbf{x}_{ub} vary slightly for each parameter. For both materials, the boundaries are set within the same ranges for L_p , $0.2 \text{ (W)} \leq L_p \leq 1.3 \text{ (W)}$, and S_s , $10 \text{ (mm/s)} \leq S_s \leq 700 \text{ (mm/s)}$. However, for S , the ranges differ: for Inconel, the range is $15 \text{ (}\mu\text{m)} \leq S \leq 28 \text{ (}\mu\text{m)}$, while for stainless steel, the range is $1 \text{ (}\mu\text{m)} \leq S \leq 42 \text{ (}\mu\text{m)}$.

Finally, Fig. 1d shows two spectral emissivity targets that serve as benchmarks to demonstrate the performance of the ALPS framework. The ideal step function spectral emissivity (top curve in Fig. 1d) represents the optimal emissivity profile that a photonic surface should exhibit for Thermophotovoltaic (TPV) applications, specifically TPV emitters as shown by Park et al. (2024). The bottom curve in Fig. 1d is the near-perfect emitter where the goal is to determine the laser parameters that yield an emissivity profile that is equal to 1 at all wavelengths (used as a benchmark in Grbic et al. (2024)). Besides these two photonic surface inverse design benchmarks, we also utilize two synthetic benchmarks to show if our approach can perform well on different inverse design problems. The additional synthetic benchmarks, as well as the algorithms used for comparison with ALPS, and all the numerical experiment setup parameters needed to reproduce this study, are thoroughly described in App. B.

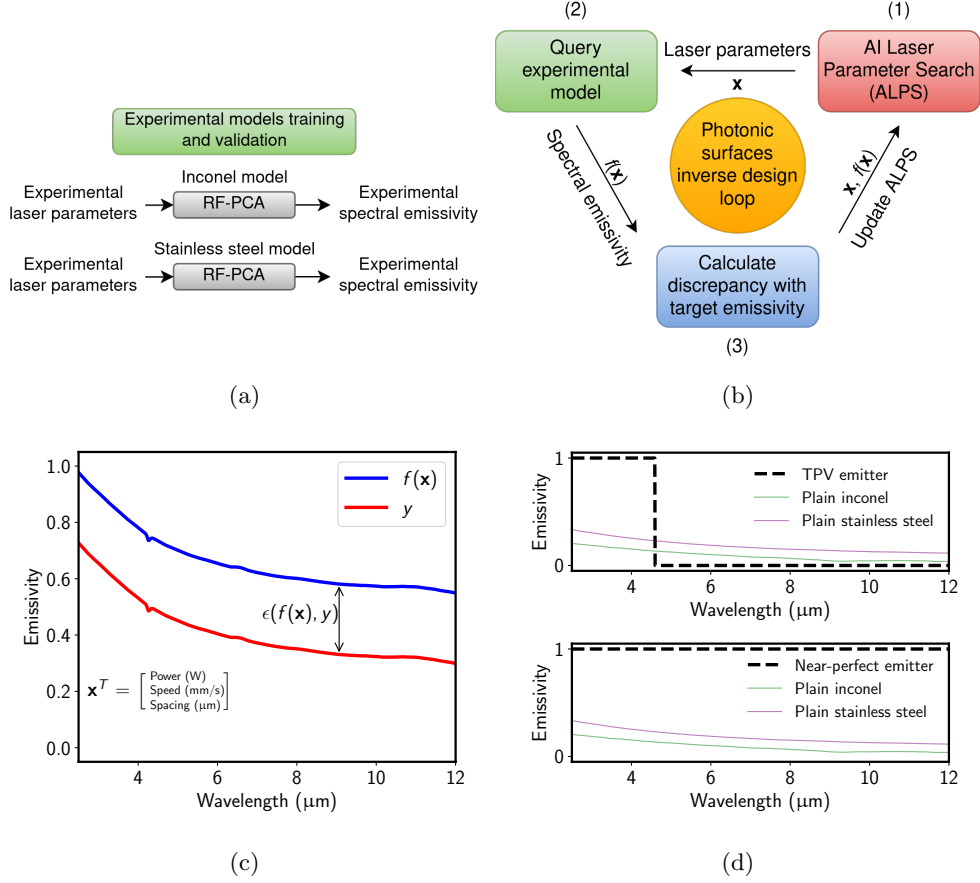


Fig. 1: Photonic surfaces inverse design segments and examples: (a) The ML experimental model pipeline developed to assess laser fabrication parameters. Each model is trained using distinct datasets and categorized according to the surface material employed for laser texturing. The RF algorithm predicts the PCA components, which are then transformed into spectral emissivity curves. (b) The inverse design loop comprises three phases: (1) Generation of laser parameters using the ALPS framework and assessment via an experimental model (defined in (a)) to produce a spectral emissivity curve (2), followed by (3) comparison of this curve against the target spectral emissivity and finally updating ALPS with new data for iterative decision making. (c) Example of the discrepancy, ϵ , as defined in Eq. (2), between the user-defined target spectral emissivity curve y and the spectral emissivity curve derived from evaluating the design vector \mathbf{x} with the model defined in (a). (d) Photonic surfaces inverse design benchmark targets: TPV emitter (top) and the near-perfect emitter (bottom). The TPV emitter target switches to 0 emissivity at a wavelength of $4.6 \mu\text{m}$. The plain spectral emissivity curves are measured from the material without laser texturing.

2.3 ALPS: AI Laser Parameter Search

ALPS plays a main role in the computational framework we have developed for photonic surface inverse design. Its task is to decide on the most informative laser parameters for experimental model evaluation to reconstruct the user-defined target vector through discrepancy minimization defined in Eq. (2). The ALPS algorithm is defined in detail in Alg. 1 with all of the required hyperparameters included.

Firstly, we consider the simpler variant of ALPS where we do not include warm starting (parameter ws is set to False). To start the inverse design process based on the user-defined target vector, we sample the design vector space using LHS, evaluate the samples using the experimental model, and train an initial RF surrogate denoted as f_{rf} . The default scikit-learn 1.2.2. hyperparameters of the RF algorithm were used (Pedregosa et al. (2011)). Note that we employed other ML algorithms as the surrogate model in ALPS, but none perform as well as RF. Selecting new design vectors to evaluate with the experimental model is done through a greedy strategy defined as prediction-based exploration by Kochenderfer and Wheeler (2019), or minimization of an interpolating surface by Jones (2001). Moreover, we extend this infill criteria or strategy by selecting a batch of design vectors, instead of a single design vector for experimental model evaluation.

The mathematical expressions defined in Eq. (4), (5) and (6), explain the procedure for selecting the best samples for experimental model evaluation. More specifically, given a matrix of samples \mathbf{X}_s generated using LHS, where each row is a vector $\mathbf{x} \in [\mathbf{x}_{lb}, \mathbf{x}_{ub}] \subset \mathbb{R}^M$, we compute the discrepancy $\epsilon(f_{rf}(\mathbf{x}), \mathbf{y})$ between the target vector $\mathbf{y} \in \mathbb{R}^N$ and the RF surrogate function f_{rf} evaluated design vector \mathbf{x} :

$$\epsilon_i = \epsilon(f_{rf}(\mathbf{x}_i), \mathbf{y}), \quad \forall \mathbf{x}_i \in \mathbf{X}_s. \quad (4)$$

To select the best n_{batch} vectors, we define \mathbf{X}_b as:

$$\mathbf{X}_b = \begin{bmatrix} \mathbf{x}^{(1)} \\ \mathbf{x}^{(2)} \\ \vdots \\ \mathbf{x}^{(n_{batch})} \end{bmatrix}, \quad (5)$$

where $\mathbf{x}^{(i)}$ are the top n_{batch} vectors from \mathbf{X}_s that minimize ϵ :

$$\mathbf{x}^{(i)} \in \arg \min_{\mathbf{x} \in \mathbf{X}_s} \epsilon(f_{rf}(\mathbf{x}), \mathbf{y}), \quad i = 1, \dots, n_{batch}. \quad (6)$$

The ϵ minimization procedure is done through a simple sorting algorithm. After the selection of \mathbf{X}_b , the RF surrogate is retrained with all of the previously sampled design vectors \mathbf{x} as well as the new batch of design vectors \mathbf{X}_b , and their respective experimental model evaluations $f(\mathbf{x})$. The process is repeated until the maximum evaluation value n_{max} is reached.

When the warm starting option of ALPS is enabled by setting the boolean parameter ws to True, we utilize a pre-trained model in conjunction with LHS, f_{ws} , for

generating initial samples, otherwise, we use LHS to generate design values within \mathbf{x}_{lb} and \mathbf{x}_{ub} . The model f_{ws} is trained and saved during a previous inverse design process, specifically for a photonic surface design aimed at a different target. We are training the surrogate model using the design vector \mathbf{x} and the corresponding experimental model value $f(\mathbf{x})$, rather than focusing on the error $\epsilon(f(\mathbf{x}), \mathbf{y})$. Therefore, $f_{ws} : \mathbb{R}^M \rightarrow \mathbb{R}^N$ is designed to capture the forward relationship between the design vectors and the target space, rather than the inverse design error landscape. This advantage opens up the potential for reusing the surrogate model after each inverse design process is completed to accelerate every subsequent process. If warm starting is enabled, the initial samples are determined with the process described in Eq. (4), (5) and (6), however, we use f_{ws} instead of f_{rf} .

Algorithm 1 AI Laser Parameter Search (ALPS)

Require: target \mathbf{y} , experimental model f , batch size n_{batch} , initial sample size n_{init} , surrogate sample size n_s , maximum evaluations n_{max} , lower boundary vector \mathbf{x}_{lb} , upper boundary vector \mathbf{x}_{ub} , warm start ws , warm start model f_{ws}

- 1: **if** ws is True **then**
- 2: $\mathbf{X}_s \leftarrow \text{LHS}(n_s, \mathbf{x}_{lb}, \mathbf{x}_{ub})$ \triangleright Generate n_s design vectors using LHS bounded by \mathbf{x}_{lb} and \mathbf{x}_{ub} and store in matrix \mathbf{X}_s
- 3: $\hat{\mathbf{X}} \leftarrow \mathbf{x}^{(i)} \in \arg \min_{\mathbf{x} \in \mathbf{X}_s} \epsilon(f_{ws}(\mathbf{x}), \mathbf{y}), \quad i = 1, \dots, n_{init}$ \triangleright Select n_{init} rows from \mathbf{X}_s based on the smallest ϵ values and store in $\hat{\mathbf{X}}$
- 4: **else**
- 5: $\hat{\mathbf{X}} \leftarrow \text{LHS}(n_{init}, \mathbf{x}_{lb}, \mathbf{x}_{ub})$ \triangleright Generate n_{init} initial design vectors using LHS bounded by \mathbf{x}_{lb} and \mathbf{x}_{ub}
- 6: **end if**
- 7: $\hat{\mathbf{F}} \leftarrow f(\hat{\mathbf{X}})$ \triangleright Evaluate each row in matrix $\hat{\mathbf{X}}$ using the experimental model f , and store in matrix $\hat{\mathbf{F}}$
- 8: $n \leftarrow \text{rows}(\hat{\mathbf{F}})$ \triangleright Number of rows in the matrix $\hat{\mathbf{F}}$
- 9: $f_{rf} \leftarrow \text{RF}(\hat{\mathbf{X}}, \hat{\mathbf{F}})$ \triangleright Train the RF surrogate f_{rf} using matrix $\hat{\mathbf{X}}$ and the responses $\hat{\mathbf{F}}$
- 10: **while** $n < n_{max}$ **do**
- 11: $\mathbf{X}_s \leftarrow \text{LHS}(n_s, \mathbf{x}_{lb}, \mathbf{x}_{ub})$ \triangleright Generate n_s design vectors using LHS bounded by \mathbf{x}_{lb} and \mathbf{x}_{ub} and store in matrix \mathbf{X}_s
- 12: $\mathbf{X}_b \leftarrow \mathbf{x}^{(i)} \in \arg \min_{\mathbf{x} \in \mathbf{X}_s} \epsilon(f_{rf}(\mathbf{x}), \mathbf{y}), \quad i = 1, \dots, n_{batch}$ \triangleright Select n_{batch} rows from \mathbf{X}_s based on the smallest ϵ values and store in \mathbf{X}_b
- 13: $f(\mathbf{X}_b)$ \triangleright Evaluate design vectors in matrix \mathbf{X}_b using the true experimental model f
- 14: $\hat{\mathbf{X}} \leftarrow \mathbf{X}_b$ \triangleright Add each row of \mathbf{X}_b into matrix $\hat{\mathbf{X}}$
- 15: $\hat{\mathbf{F}} \leftarrow f(\mathbf{X}_b)$ \triangleright Add each response of $f(\mathbf{X}_b)$ into matrix $\hat{\mathbf{F}}$
- 16: $f_{rf} \leftarrow \text{RF}(\hat{\mathbf{X}}, \hat{\mathbf{F}})$ \triangleright Retrain f_{rf} with the updated $\hat{\mathbf{X}}$ and the true responses $\hat{\mathbf{F}}$
- 17: $n \leftarrow \text{rows}(\hat{\mathbf{F}})$ \triangleright Update n
- 18: **end while**
- 19: $\hat{\epsilon} \leftarrow \epsilon(\mathbf{y}, \hat{\mathbf{F}})$ \triangleright Obtain discrepancy array $\hat{\epsilon}$ based on target \mathbf{y} and all values in $\hat{\mathbf{F}}$ i.e., apply Eq. (2) for each value in $\hat{\mathbf{F}}$
- 20: $\mathbf{x}_{best} \leftarrow \text{row corresponding to the smallest value of } \hat{\epsilon} \text{ in } \hat{\mathbf{X}}$ \triangleright Select the best row from $\hat{\mathbf{X}}$ based on the smallest $\hat{\epsilon}$ value

3 Results

In this section, we present the ALPS framework results for the two photonic surface inverse design benchmarks (Fig. 1d) and two synthetic benchmarks (Fig. B4b). ALPS is compared to other optimization algorithms such as Particle Swarm Optimization (PSO), DE, Mesh Adaptive Direct Search (MADS), Nelder Mead (NM), Limited memory Broyden–Fletcher–Goldfarb–Shanno with Boundaries (LBFGSB), and BO. We also include a simple random sampling algorithm for comparison (denoted as Random). The specifics and hyperparameters of these algorithms are detailed in App. B.2 (Tab. B2).

We also showcase the major benefit of using ALPS with warm starting for inverse design by demonstrating its capability of cross-target and cross-material inverse design optimization. For all numerical experiments only 100 experimental model evaluations (denoted as Experiments) are considered, i.e., the $n_{max} = 100$. Other ALPS-specific parameters used for all benchmarks and comparisons are $n_{batch} = 5$, $n_{init} = 5$, and $n_s = 600$ (for hyperparameter details see Alg. 1).

To rigorously assess the performance of optimization algorithms across all benchmarks, we execute each algorithm for 100 repeated runs. Throughout each run, we monitor the error value (ϵ), as defined in Eq. (2), during each of the 100 experimental model evaluations. For these evaluations, we track the "best found so far" value of ϵ , updating this record only if a lower ϵ value is discovered during subsequent evaluations. This progressive update of the minimum ϵ forms the basis of our convergence graphs, which illustrate the optimization progress over time. At the end of the trials, we analyze these results by calculating the mean, and the 10th and 90th percentiles, of these minimum values across the 100 repetitions, providing insights into the algorithms' efficiency and performance variability.

In order to visualize the quality of the solutions generated by each optimization algorithm, we obtain the best design vectors found for each of the 100 repeated runs and we use them as inputs to our benchmark models to obtain the corresponding curves. We average these solutions and calculate the 10th and 90th percentiles and visualize them juxtaposed with the target. We denote these graphs as solution reconstruction graphs.

3.1 Synthetic Benchmarks Results

In Fig. 2, we present the results of the three-dimensional logistic growth and four-dimensional sinusoidal oscillation with damping benchmarks. Specifically, Fig. 2a displays the convergence graphs for all evaluated optimization algorithms, while Fig. 2b showcases the logistic growth benchmark solution reconstruction graph. It is evident that for the logistic growth benchmark, ALPS solutions cluster tightly around the target value, reflecting the reduced uncertainty in the inverse design. The ALPS mean and standard deviation of the ϵ value for the logistic growth benchmark after 100 repeated runs are 13.52, and 9.03, respectively. The second best performing algorithm is PSO with the mean of ϵ as 26.20 and standard deviation 16.14.

Fig. 2c and 2d show the convergence graphs for all algorithms and the ALPS-reconstructed solution graph for the sinusoidal oscillation with damping benchmark, respectively. The ALPS algorithm outperforms all other optimization algorithms; however, NM and BO are the second and third best, with significantly better accuracy than the rest. The reconstructed ALPS solution closely aligns with the target design, but the uncertainty remains slightly higher across 100 repeated runs compared to that of the logistic growth benchmark target. The ALPS mean and standard deviation for ϵ for the sinusoidal oscillation with damping benchmark are 0.25 and 0.11, while the second and third best, NM and BO, have the values 0.30 and 0.26, and 0.31 and 0.13, respectively.

Detailed statistics from all repeated runs are provided in Tab. C3 and C4, which cover logistic growth and sinusoidal oscillation with damping, respectively. For the

logistic growth benchmark, ALPS demonstrates superior performance in terms of both accuracy and reliability, as it exhibits the best mean and standard deviation across the 100 repeated runs. However, the minimal error is achieved by NM, which, despite obtaining the lowest error, exhibits the largest standard deviation, indicating no reliability. In the case of sinusoidal oscillation with damping, ALPS also excels by showing the lowest mean error and one of the lowest standard deviations in the final model evaluation. Although NM finds the best solution, it proves to be the least reliable, heavily dependent on the initial random design point.

Further in-depth convergence graphs and solution reconstruction graphs of both benchmarks are available in App. C.1. Figure C5 provides convergence graphs for all algorithms across both benchmarks, incorporating measures of uncertainty. Fig. C6 and C7 present the solution reconstruction graphs for the logistic growth and sinusoidal oscillation with damping benchmarks, respectively.

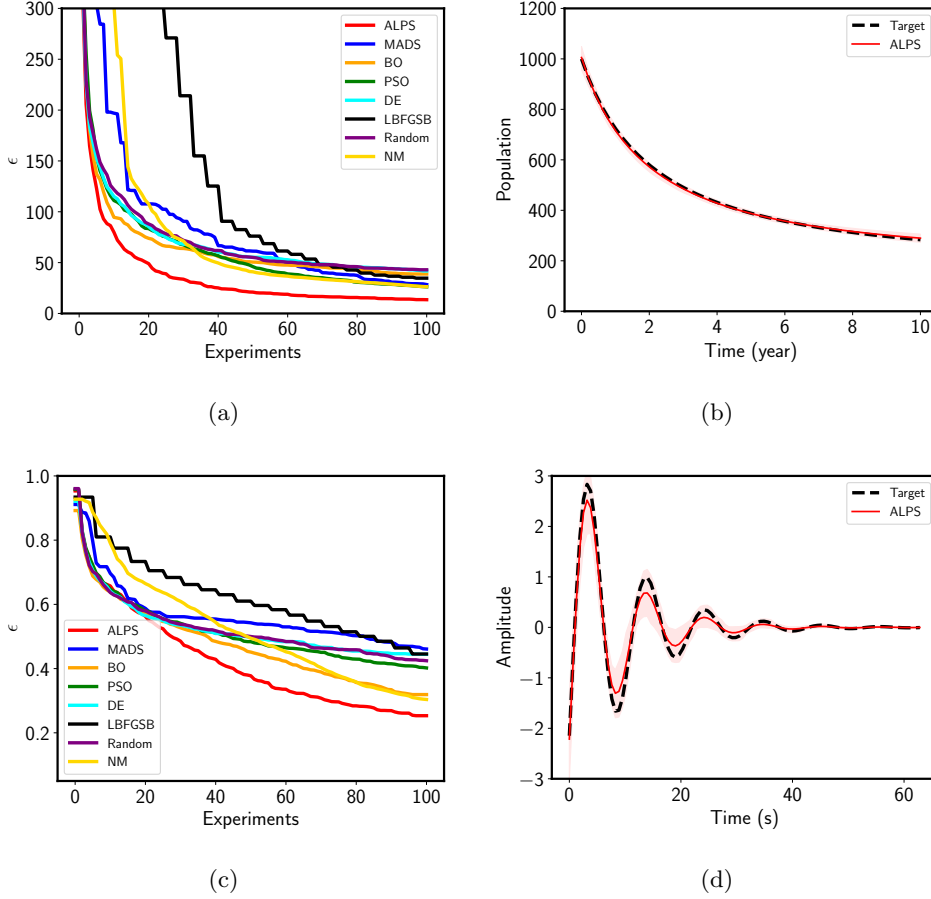


Fig. 2: The inverse design results for the logistic growth (top) and sinusoidal oscillation with damping (bottom) benchmarks: (a) Convergence graphs for all optimization algorithms for the logistic growth benchmark. (b) ALPS solution reconstruction graph for the logistic growth benchmark. (c) Convergence graphs for all optimization algorithms for the sinusoidal oscillation with damping benchmark. (d) ALPS solution reconstruction graph for the sinusoidal oscillation with damping benchmark.

3.2 Photonic Surfaces Design Results

Fig. 3 and Fig. 4 show the results of the photonic surface inverse design benchmarks. The first column (Fig. 3a and 3c, and Fig. 4a and 4c) shows the convergence graphs of the Inconel near-perfect emitter, Inconel TPV emitter, Stainless steel near-perfect emitter, and Stainless steel TPV emitter, respectively. The second column of both figures (Fig. 3b and 3d, and Fig. 4b and 4d) shows, in the same order, the ALPS solution reconstruction graphs as it is the best performing algorithm for all of the target values. Moreover, in contrast to the synthetic benchmarks, the performance of

NM on the photonic surface inverse design is poor. Convergence graphs with uncertainty can be found in the App. C.2, Fig. C8. The near-perfect emitter reconstructed solutions are extremely close to the target values (for both Inconel and Stainless steel benchmarks), however, the TPV emitter solution reconstruction shows that it is not possible to fully approximate the target. This approximation could be potentially improved by including additional design space parameters, i.e., additional laser fabrication parameters.

Compared to other optimization methods, ALPS exhibits quicker convergence. For a real experimental setting, this is extremely beneficial as the main goal is to achieve inverse design with minimal usage of experimental resources. Most optimization algorithms are able to converge to satisfying solutions (shown in Fig. C9-C12) (with the exception of NM, and LBFGB, that are highly sensitive to the initial condition). However, similarly as for the synthetic benchmarks, ALPS exhibits reliability and consistency as it has an overall lowest uncertainty across all benchmarks (see detailed convergence statistics for all runs presented in Tab. C5-C8). Generally, this property of the optimization algorithm is ideal when only a low number of evaluations are allowed and multiple repeated trials are not possible.

For the Inconel near-perfect emitter target, the ALPS mean ϵ is 0.02, which is the same as PSO, however, the standard deviation of ϵ for ALPS is 0.003, while it is 0.01 for PSO. For the Inconel TPV emitter target, the ALPS mean and standard deviation of ϵ are 0.30 and 0.003, respectively, while the second and third best are the PSO and BO algorithms, with 0.31 and 0.01, and 0.31 and 0.02 mean and standard deviation for ϵ , respectively. For the Stainless steel near-perfect emitter, ALPS mean and standard deviation of ϵ are 0.02 and 0.004 which is the same as PSO. BO is the second best performing algorithm for this case having achieved the same mean, but a larger standard deviation of 0.02.

The final target of the photonic surface benchmark, the Stainless steel TPV emitter, is not a hard challenge for most optimization algorithms, as ALPS, BO, PSO, DE and even random sampling have the same ϵ value, and are the same in all other metrics, except for the maximum ϵ value obtained in the 100 repeated runs, where the lowest is found by ALPS with 0.30. Finally, the mean ϵ values for the top three optimization algorithms (ALPS, BO, PSO) are comparable after 100 experimental model evaluations for all benchmarks. However, a significant advantage of ALPS is its ability to accurately infer laser parameters with as few as 20 to 50 experimental model evaluations, as demonstrated in the first column of Fig. 3 and Fig. 4, i.e., ALPS finds better solutions faster than all other algorithms. For all these analyses we used a set of unoptimized ALPS and out-of-the-box RF algorithm hyperparameters, however, a detailed analysis on how these parameters influence the performance of ALPS is given in App. C.3.

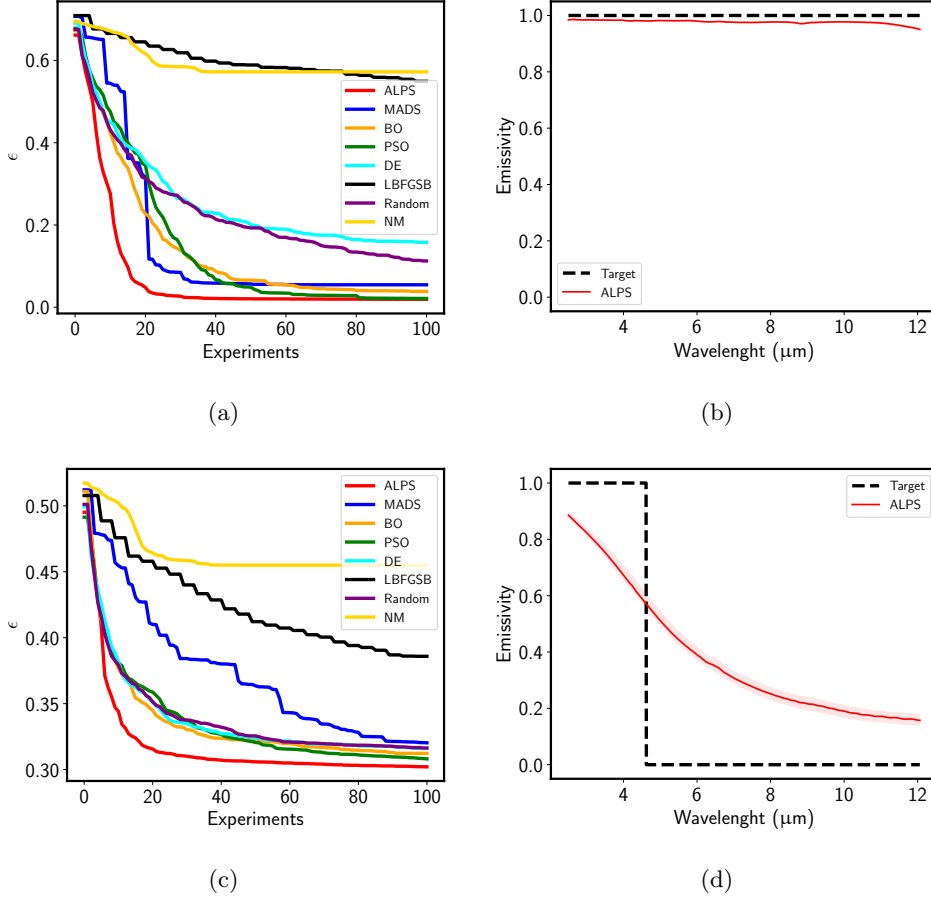


Fig. 3: The inverse design results for the Inconel photonic surface benchmarks. Convergence graphs for all optimization algorithms are shown in the first column, while in the second, ALPS solution reconstruction graphs are shown: (a) Convergence graphs for the Inconel near-perfect emitter target benchmark. (b) ALPS solution reconstruction graph for the Inconel near-perfect emitter benchmark. (c) Convergence graphs for the Inconel TPV emitter target benchmark. (d) ALPS solution reconstruction graph for the Inconel TPV emitter.

3.3 Photonic Surfaces Design with Warm Starting

We employ two strategies to accelerate the convergence of ALPS through warm starting. The first strategy, termed cross-target warm starting, uses a model derived from a previous inverse design process with a different target, more specifically, the same material is used but a different target shape. The second, cross-material warm starting, utilizes a model from a prior process where both the target shape and the material differed. As outlined in Alg. 1, these pre-trained models are used for generating initial

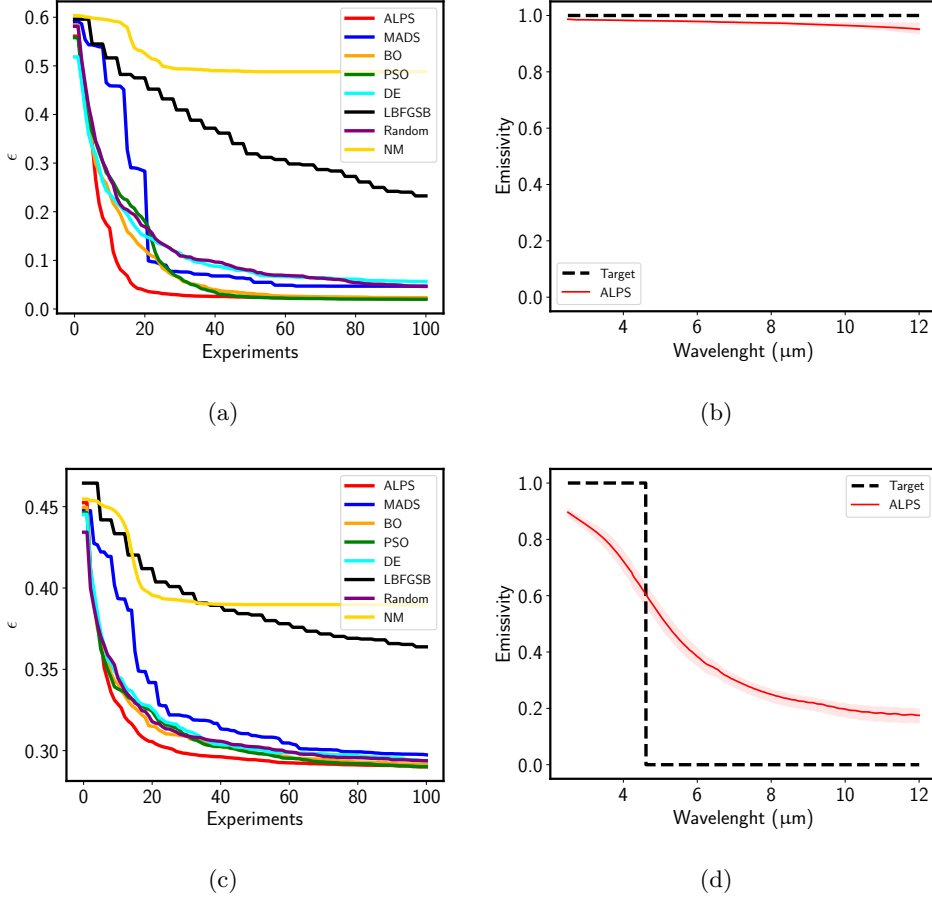


Fig. 4: The inverse design results for the Stainless steel photonic surface benchmarks. Convergence graphs for all optimization algorithms are shown in the first column, while in the second, ALPS solution reconstruction graphs are shown: (a) Convergence graphs for the Stainless steel near-perfect emitter target benchmark. (b) ALPS solution reconstruction graph for the Stainless steel near-perfect emitter benchmark. (c) Convergence graphs for the Stainless steel TPV emitter target benchmark. (d) ALPS solution reconstruction graph for the Stainless steel TPV emitter.

samples instead of the LHS method. These samples are then used to train an initial RF surrogate which is further used in the main ALPS loop.

To demonstrate the effectiveness and versatility of ALPS with both cross-target and cross-material warm starting, we conduct a comparative analysis against ALPS without warm starting using our photonic surface inverse design benchmark. We perform 100 runs for each target to generate the convergence graphs. Each run limits the experimental model evaluations to 100. Additionally, prior to running of ALPS with

warm starting, we run the ALPS without warm starting on the different target to generate the model that is used for initializing samples. This generated model is subsequently used for warm starting each ALPS run. This procedure is included in every of the 100 repeated runs for each target to mitigate any variability in the performance of the prior warm starting models.

Fig. 5 and Fig. 6 show the convergence graphs and the solution reconstruction graphs of both ALPS with and without cross-target warm starting for Inconel and Stainless steel, respectively. As an example, when the Inconel TPV emitter is used as the target, ALPS is warm started by a model that is generated after an inverse design of the Inconel near-perfect emitter, and vice-versa. From the convergence graphs (Fig. 5a and 6a, and Fig. 5c and 6c) it can be seen that for all cases the warm started variant of ALPS (denoted as $ALPS_{ws=True}$) performs better than the ALPS without warm starting. When the targets are Inconel near-perfect emitter, Inconel TPV emitter and Stainless steel near-perfect emitter (top rows of Fig. 5 and 6), ALPS with warm starting can approximate the target in 10 to 20 experimental model evaluations. For the Stainless steel TPV emitter target, the ALPS with warm starting is slightly better than the ALPS without warm starting. However, after 100 experimental model evaluations, all variants converge to the approximately the same design. Detailed convergence statistics of all runs are available in App. C.4, more specifically, Tab. C17-C24.

Fig. 7 and Fig. 8 show the convergence and solution reconstruction graphs for ALPS with and without cross-material warm starting. In this case, additionally to switching to a different inverse design target, we also include switching to a different material, i.e., when the Stainless steel near-perfect emitter is the target, ALPS is warm started by a model that is generated after an inverse design of the Inconel TPV emitter, and vice-versa. The convergence graphs in the first column of Fig. 7 and 8 show that cross-material warm starting can be very beneficial (Fig. 7a and Fig. 8a), or it can either bring no significant boost in performance (Fig. 7c), or even slightly worsen the performance (Fig. 8c). The worsened performance of ALPS with warm starting for the Stainless steel TPV emitter target can be explained with the difference between lower and upper bound difference of the spacing parameter of the experimental models between Inconel and Stainless steel. The best found laser parameters for the Stainless steel TPV target by the ALPS model without warm starting are 0.9 W for laser power, 338 mm/s for scanning speed, and 3.37 μm for the spacing. The spacing domain for the Inconel experimental model ranges from 15 μm to 28 μm , as shown in Fig. A2. Therefore, the initial solutions generated by the warm starting model are limited to laser parameters within this range. In this context, employing LHS is advantageous as it provides an unbiased approach, enabling the uniform generation of initial samples across the entire spacing domain.

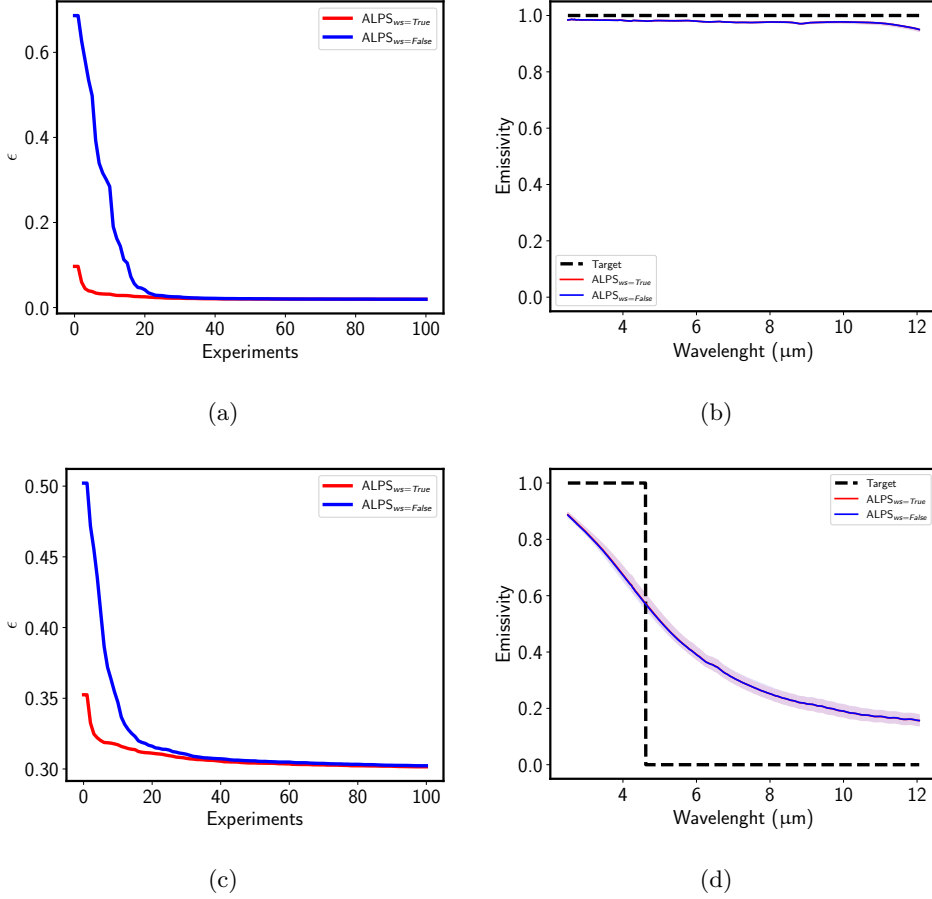


Fig. 5: The inverse design results of ALPS with and without cross-target warm starting for the photonic surface benchmarks ($ALPS_{ws=True}$ means ALPS with warm starting and is shown as the red line). Convergence graphs are shown in the first column, while in the second, the solution reconstruction graphs are shown: (a) Convergence graphs for the Inconel near-perfect emitter target benchmark. (b) Solution reconstruction graph for the Inconel near-perfect emitter benchmark. (c) Convergence graphs for the Inconel TPV emitter target benchmark. (d) Solution reconstruction graph for the Inconel TPV emitter.

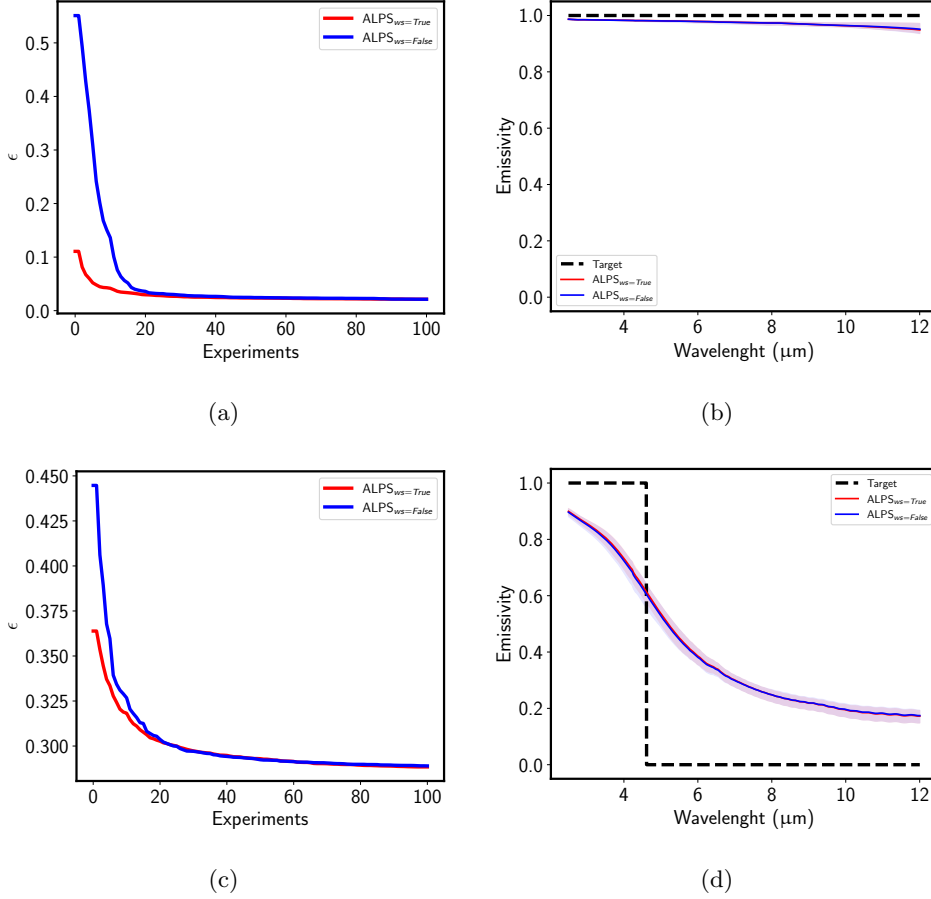


Fig. 6: The inverse design results of ALPS with and without cross-target warm starting for the photonic surface benchmarks ($ALPS_{ws=True}$ means ALPS with warm starting and is shown as the red line). Convergence graphs are shown in the first column, while in the second, the solution reconstruction graphs are shown: (a) Convergence graphs for the Stainless steel near-perfect emitter target benchmark. (b) Solution reconstruction graph for the Stainless steel near-perfect emitter. (c) Convergence graphs for the Stainless steel TPV emitter target benchmark. (d) Solution reconstruction graph for the Stainless steel TPV emitter.

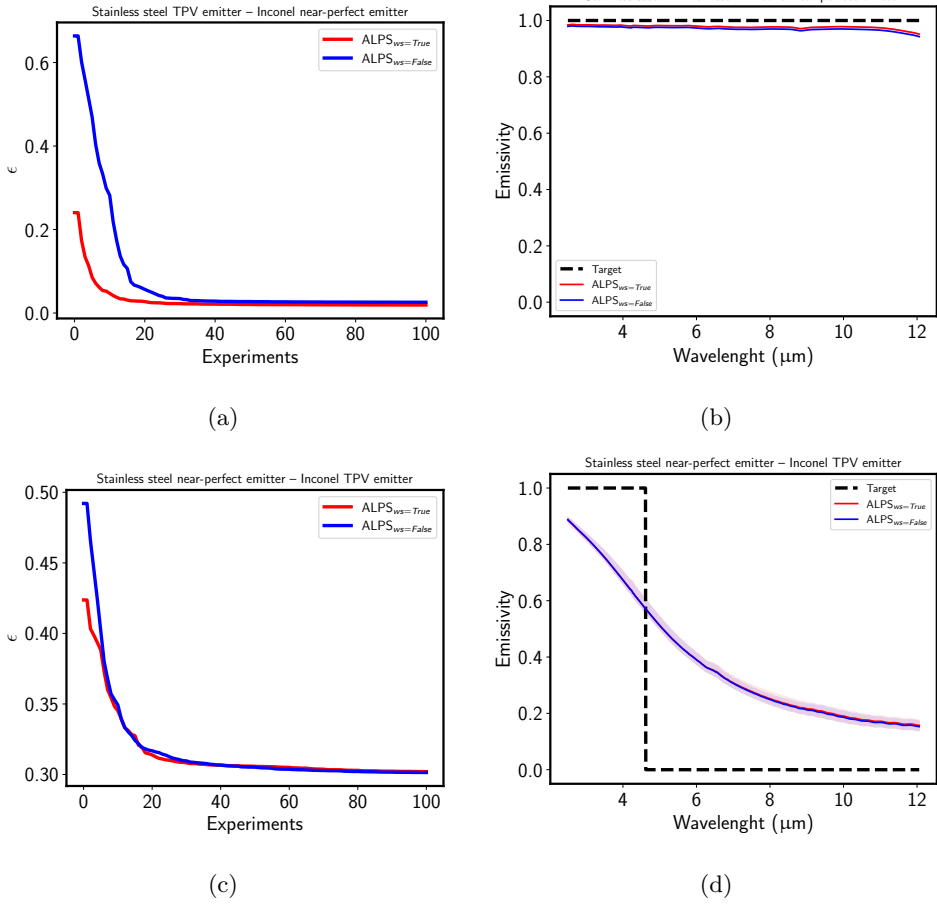


Fig. 7: The inverse design results of ALPS with and without cross-material and cross-target warm starting for the photonic surface benchmarks ($ALPS_{ws=True}$ means ALPS with warm starting and is shown as the red line). The title of each graph presents the warm starting model source (stated first) and inverse design target (stated last). Convergence graphs are shown in the first column, while in the second, the solution reconstruction graphs are shown: (a) Convergence graphs for the Inconel near-perfect emitter target benchmark. (b) Solution reconstruction graph for the Inconel near-perfect emitter benchmark. (c) Convergence graphs for the Inconel TPV emitter target benchmark. (d) Solution reconstruction graph for the Inconel TPV emitter benchmark.

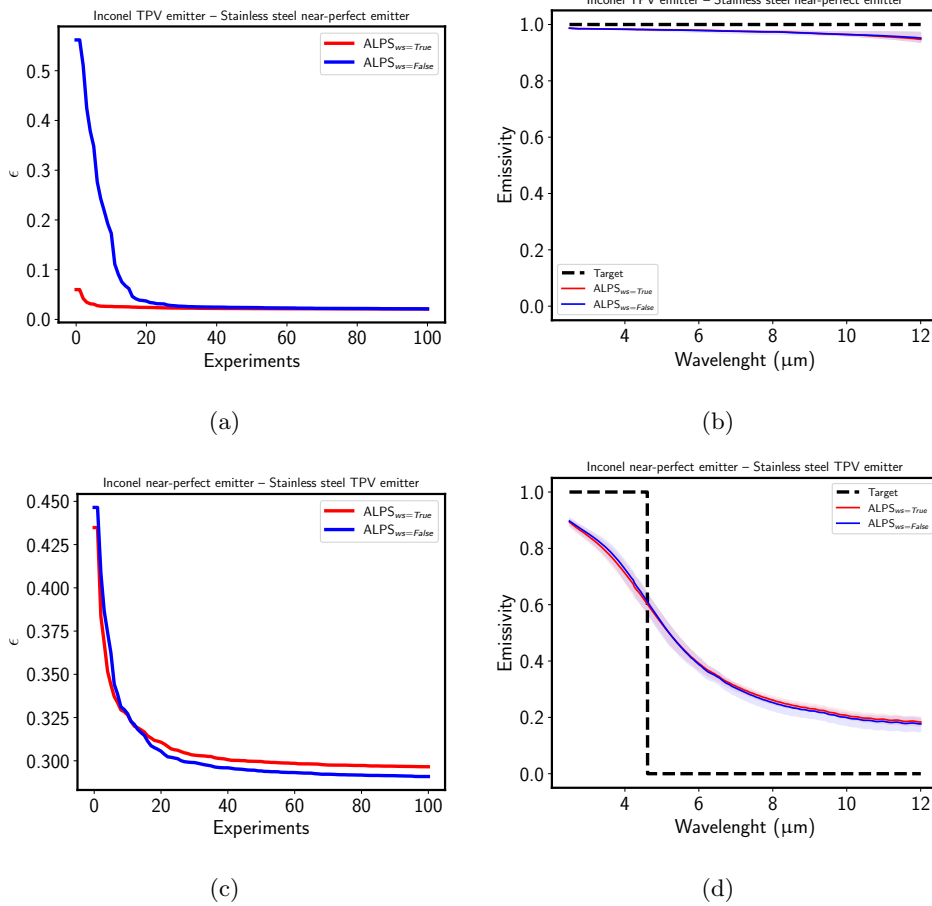


Fig. 8: The inverse design results of ALPS with and without cross-material and cross-target warm starting for the photonic surfaces benchmarks ($ALPS_{ws=True}$ means ALPS with warm starting and is shown as the red line). The title of each graph presents the warm starting model source (stated first) and inverse design target (stated last). Convergence graphs are shown in the first column, while in the second, the solutions reconstruction graphs are shown: (a) Convergence graphs for the Stainless steel near-perfect emitter target benchmark. (b) Solution reconstruction graph for the Stainless steel near-perfect emitter. (c) Convergence graphs for the Stainless steel TPV emitter target benchmark. (d) Solution reconstruction graph for the Stainless steel TPV emitter.

4 Conclusion

We introduce and investigate the ALPS algorithm, developed for the inverse design of photonic surfaces. ALPS utilizes a greedy surrogate sampling method, employing the RF algorithm as a surrogate, and has demonstrated superior performance over established optimization algorithms in all benchmark tests. Notably, ALPS offers reliable convergence with limited experimental model evaluations, a significant advantage in photonic surface inverse design practical applications. Additionally, its capability for cross-target and cross-material warm starting enhances its utility in repetitive design processes across similar or identical design spaces. Future research could explore the application of ALPS in real-world autonomous experimental settings for further advancing photonic surface design, as well as generalizing the proposed approach to other problem settings.

Acknowledgments

This work was supported by the Laboratory Directed Research and Development Program of Lawrence Berkeley National Laboratory under U.S. Department of Energy Contract No. DE-AC02-05CH11231. Müller’s time was supported under U.S. Department of Energy Contract No. DE-AC36-08GO28308, U.S. Department of Energy Office of Science, Office of Advanced Scientific Computing Research, Scientific Discovery through Advanced Computing (SciDAC) program through the FASTMath Institute to the National Renewable Energy Laboratory.

Author Contributions

L.G. wrote the manuscript, developed the methods, developed the code, designed the numerical experiments, and analyzed the performance of the algorithms, M.P. provided the experimental data and edited the manuscript, J.M. supervised the research and edited the manuscript, V.Z. and W.A.J. supervised the research, provided funding and edited the manuscript.

Declaration of Competing Interest

The authors declare that they have no known competing financial interests or personal relationships that could have appeared to influence the work reported in this paper.

Data Availability

The machine learning models, data and benchmarks needed to reproduce the study can be found on the following repository: <https://github.com/lukagrbic/ALPS-Data>

Appendix A Experimental Datasets and Model

In this section we describe the experimental dataset used to train the experimental models used to assess the performance of our methods. We also include the details of the RF-PCA algorithm, the model validation procedures and assess the accuracy of the models.

A.1 RF-PCA Algorithm

The experimental model is based on a combination of the RF algorithm and the PCA algorithm used to compress the large dimensionality of the spectral emissivity space. The RF algorithm (introduced by [Breiman \(2001\)](#)) is an ensemble learning method for ML classification and regression. It constructs randomly defined decision trees during training, outputting the mean prediction of individual trees. This randomness, introduced by selecting a subset of features for each tree split, helps de-correlate trees, reducing overfitting and allowing for interpretability. It is particularly suited for modeling problems that have well structured features like laser fabrication parameters.

The RF-PCA algorithm comprises two main parts, each with its own pipeline, as shown in [Fig. A1](#). Initially, the PCA model is trained to convert spectral emissivity curves into ten-dimensional PCA components. Subsequently, the RF model is trained using laser parameters to predict these PCA components. The PCA model is then employed to inversely transform these predictions back into the spectral emissivity space, thus modeling the relationship between the laser parameters and spectral emissivity. This approach builds on the results discussed in our earlier publication ([Grbcic et al. \(2024\)](#)). It is important to clarify that incorporating the PCA model is not essential for accurately modeling the relationship between laser parameters and spectral emissivity. Rather, the primary function of PCA compression is to enhance the computational efficiency of the entire experimental model and to significantly decrease the storage size of the experimental model used for generating function evaluations in our ALPS numerical experiments.

The Python module scikit-learn 1.2.2. implementation of both the RF and PCA algorithms were used to train the experimental models ([Pedregosa et al. \(2011\)](#)). Most hyperparameters of the RF algorithm are set to default values, however, the number of estimators (trees) was set to 450, and the max depth value was set to 10, as they are determined to be optimal for this task through numerical experimentation.

A.2 Experimental Datasets

[Fig. A2](#) illustrates the experimental dataset distributions for both materials, namely Inconel and Stainless steel. The laser fabrication parameter space distribution of dataset instances for the Stainless steel material can be observed in [Fig. A2a](#), while [Fig. A2b](#) displays the Inconel dataset distribution. All data instances are color-coded based on their corresponding average emissivity values across the wavelength domain (2.5 μm to 12 μm). The total number of data points in the Stainless steel dataset is 35,326, whereas in the Inconel dataset, it is 11,759. The range of the spacing parameter in the Inconel dataset is narrower than that of the Stainless steel dataset, and the Stainless steel dataset exhibits a higher overall average emissivity value (computed as

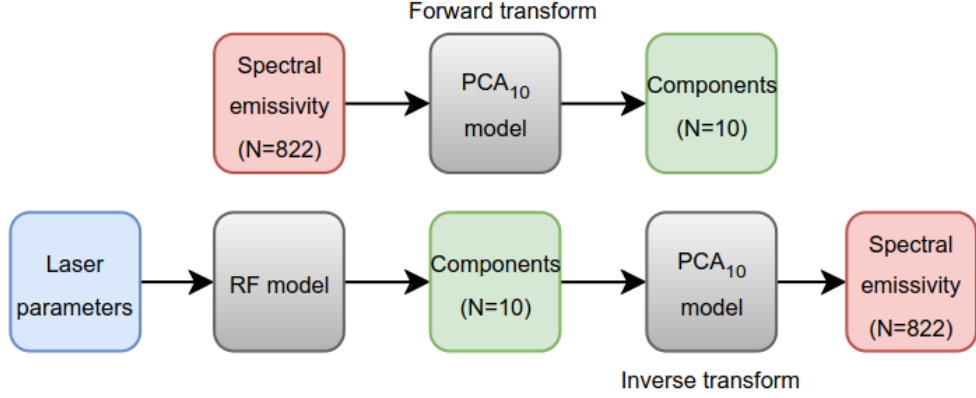


Fig. A1: The RF-PCA algorithm is employed to train the experimental models. The top section of the figure illustrates the PCA model’s pipeline (PCA₁₀ implies that the model transforms inputs into 10 components), which processes spectral emissivity values and converts them into a ten-dimensional principal component space. The bottom section depicts the complete RF-PCA model pipeline, where laser parameters serve as inputs to the RF model to predict PCA components. These components are then inversely transformed back into the spectral emissivity space.

the average of all instances’ individual average emissivities) compared to the Inconel dataset. The experimental sampling for both datasets is uniform and thoroughly covers the entire laser parameter space.

Fig. A2c presents a subset of the Stainless steel dataset with the range of the spacing parameter constrained to match that of the Inconel dataset. This comparison aims to highlight the resemblance between the two datasets. It is observed that there are similarities in the gradient of the average emissivity across the laser fabrication space. However, it is noteworthy that the average emissivity of the Stainless steel dataset remains higher (0.428) compared to that of the Inconel dataset (0.336). The similarity of the gradient potentially implies that using a pretrained model for Stainless steel could be used for warm starting the photonic surface inverse design process that is based on the Inconel material.

For full details of the experimental procedure that is used to generate these datasets, readers are encouraged to refer to our prior publications (Park et al. (2024) and Grbcic et al. (2024)).

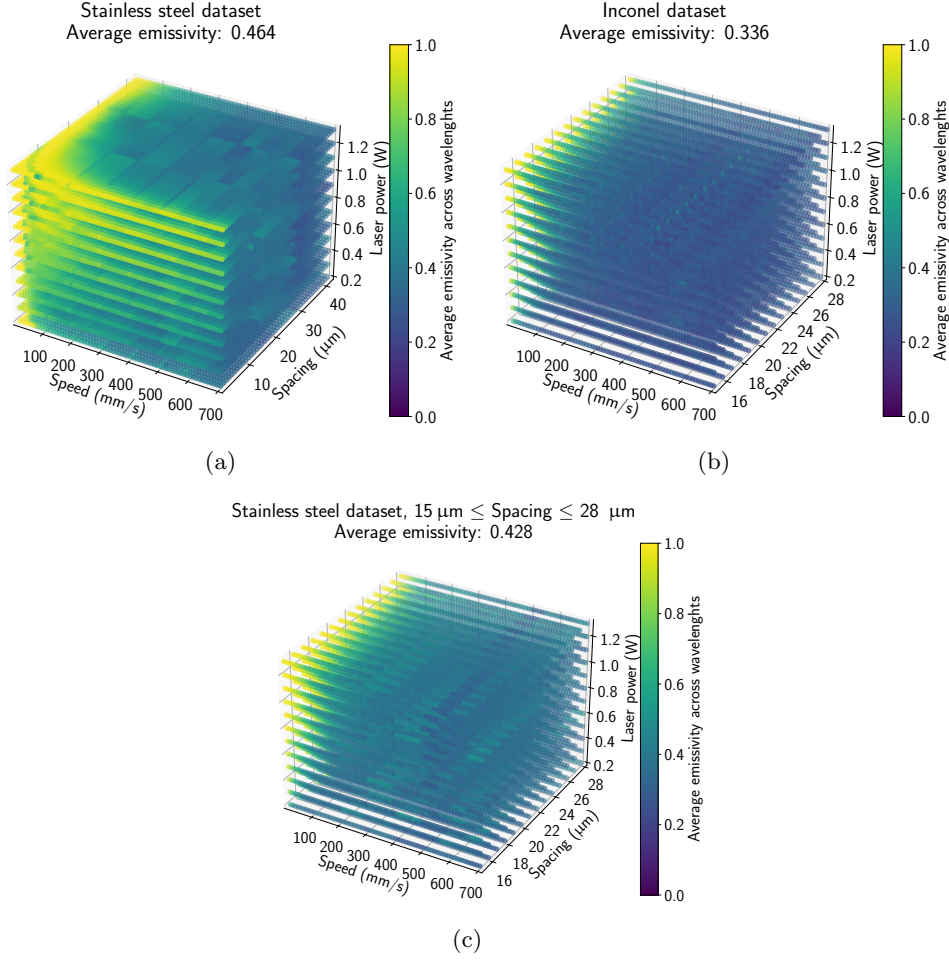


Fig. A2: Experimental dataset distributions in laser fabrication parameter space, colored by the average emissivity value across all wavelengths for all data: (a) Stainless steel dataset where the total number of data is 35,326. (b) Inconel dataset where the total number of data is 11,759. (c) Subset of the Stainless steel dataset using only the same range for the spacing parameter as the Inconel dataset to showcase similarity.

A.3 Experimental Models Validation

To train and validate the experimental models, we randomly selected 20,000 instances from the entire Stainless steel dataset and 11,000 instances from the Inconel dataset. Utilizing the whole dataset to train the models is not considered since an increase in data yields an increase in the storage space of the models. We divided each dataset into 75% for training and 25% for testing. Next, we conducted a learning curve analysis on the 75% of the training dataset using a K-fold ($K = 3$) cross-validation method to

assess the accuracy and uncertainty of the predictions of both models. The primary metric used to assess the models is the RMSE (defined in Eq. (3)).

Fig. A3 presents the outcomes of the analysis for both models. Fig. A3a displays the learning curves for both models, illustrating the impact of varying dataset sizes—25%, 50%, 75%, and 100% of the training set (75% of the whole dataset)—on model accuracy through a cross-validation analysis. The results indicate that increasing the dataset size does not significantly enhance the accuracy of either model. The Stainless Steel model exhibits a marginally higher RMSE, which may be attributed to a broader range in laser parameter space (i.e., a larger range of the spacing parameter). Fig. A3b depicts the results obtained when the entirety of the training data (75% of the whole dataset) is used to train the models, and the testing data (25% of the whole dataset) is utilized for model assessment. This is illustrated through a histogram of RMSE values derived from comparing the model predictions against the test set instances. For both models, the majority of RMSE values are concentrated below 5%. The Stainless Steel model has average, maximum, and standard deviation RMSE values of 2.3%, 24.0%, and 1.8%, respectively. For the Inconel model, these values are 1.6%, 14.4%, and 1.4%. Although the maximum RMSE values indicate poor performance on some outliers, the models generally demonstrate excellent performance based on their average RMSE values. The models that are used for inference during the ALPS process are trained only with the training set (75% of each selected experimental dataset) to further reduce the storage size of the models.

Finally, we evaluated the accuracy of the PCA model for reconstructing spectral emissivity. The spectral emissivity curves from the training set are utilized to train the PCA model with 10 components. The trained PCA model then transformed the test set spectral emissivity curves into a ten-dimensional principal component space. These components are subsequently inversely transformed back to the spectral emissivity space and compared with the original curves from the test set using RMSE. The average RMSE for the Stainless steel PCA model (calculated by averaging the RMSE between each test set instance and its PCA reconstruction) is 0.08%, and for the Inconel model, it is 0.074%. These extremely low RMSE values suggest that the PCA model effectively compresses the spectral emissivity curves.

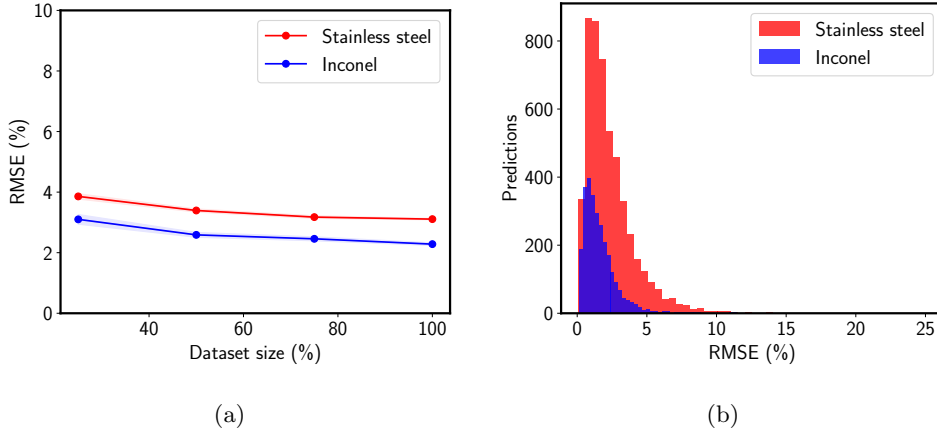


Fig. A3: Results of the RF-PCA experimental model validation: (a) Learning curve of both Stainless steel and Inconel models. (b) Histogram visualization of RMSE values for each predicted instance when compared to the testing set instances.

Appendix B Synthetic Benchmarks and Numerical Experiments Setup

In this section, we introduce the supplementary inverse design synthetic benchmarks employed to evaluate the performance of the ALPS algorithm and its comparison against other optimization techniques. Additionally, we detail the algorithms selected for comparison, including their implementation specifics and hyperparameters.

B.1 Synthetic Benchmarks

The reason for inclusion of inverse design synthetic benchmarks is to showcase that the ALPS approach generalizes beyond the photonic surface inverse design problem. Fig. B4 shows the two additional targets, namely the sinusoidal oscillation with damping model and the logistic growth model used for population modeling. These synthetic benchmarks are chosen since the target value is a curve that is parameterized with a low dimensional design vector, similarly to the photonic surface inverse design benchmarks. Both synthetic benchmarks are defined through the inverse design mathematical framework presented in Eq. (1), (2) and (3).

The mathematical expression for the sinusoidal oscillator with damping is defined in Eq. (B1) as:

$$\mathbf{y} = A(t) = a \cdot e^{-\beta \cdot t} \cdot \sin(\gamma \cdot t + \phi) \quad (\text{B1})$$

where a , β , γ , and ϕ are the model coefficients that need to be determined in order to reconstruct the target vector \mathbf{y} (displayed in Fig. B4a with the coefficient values).

For this case, the design vector is $\mathbf{x} = [a, \beta, \gamma, \phi]^T$. The amplitude A is discretized with 100 time steps t in the domain from 0 to 20π .

The mathematical expression for the logistic growth model is defined in Eq. (B2) as:

$$\mathbf{y} = P(t) = \frac{K}{1 + \left(\frac{K-P_0}{P_0}\right) \cdot e^{-r \cdot t}} \quad (\text{B2})$$

where K , P_0 , and r are model coefficients (values annotated in Fig. B4b) that define the design vector $\mathbf{x} = [K, P_0, r]^T$. The population P target value vector is discretized using 50 points of time t with a total range from 0 to 10 years, i.e. the target vector \mathbf{y} has 50 components. The lower and upper boundaries for inverse design optimization (Eq. (2)) of the sinusoidal oscillation with damping and the logistic growth model, \mathbf{x}_{lb} and \mathbf{x}_{ub} , are defined in Tab. B1.

Table B1: The lower and upper bounds of the inverse design optimization problem, \mathbf{x}_{lb} and \mathbf{x}_{ub} , respectively, for both synthetic benchmarks (defined in the first column).

Synthetic benchmark	\mathbf{x}_{lb}	\mathbf{x}_{ub}
Sinusoidal oscillation	$a = 2, \beta = 0.05, \gamma = 0, \phi = 3$	$a = 5, \beta = 0.4, \gamma = 2, \phi = 15$
Logistic growth	$K = 100, P_0 = 100, r = 0.01$	$K = 1200, P_0 = 1400, r = 0.4$

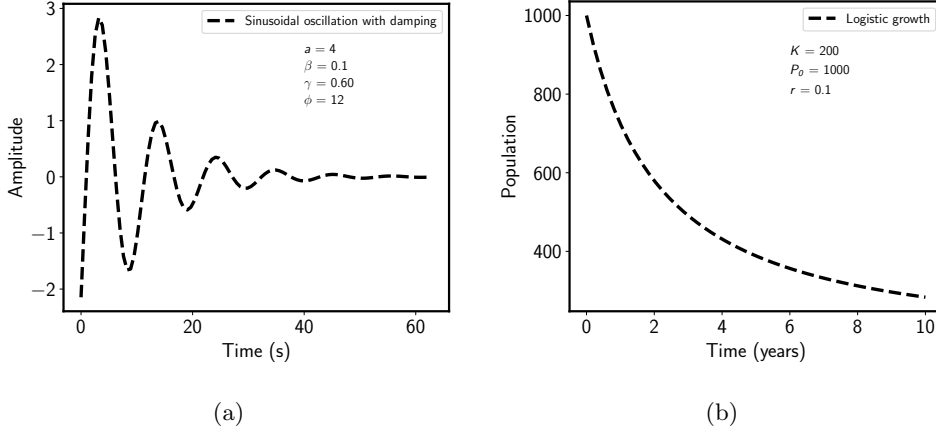


Fig. B4: The synthetic benchmark targets with annotated model coefficients needed to reconstruct them: (a) The sinusoidal oscillation with damping model. (b) The logistic growth model.

B.2 Algorithms used for Comparison

To highlight the performance of ALPS, we conduct a comparative analysis with other established algorithms from various optimization algorithm categories. From the population-based algorithms category, we select PSO and DE (Kennedy and Eberhart (1995), Storn and Price (1997)). Mesh Adaptive MADS and NM are chosen from the direct search algorithms category (Audet and Dennis Jr (2006), Lagarias et al. (1998)). L-BFGS-B is included as a representative of the gradient-based algorithms, while BO is a the model-based optimizer (Shahriari et al. (2015)).

Table B2: The optimization algorithms and their corresponding categories, that are used for comparison with ALPS on the photonic surface inverse design problem, as well as the two synthetic benchmark problems.

Algorithm	Category	Python module
PSO	Population-based	Indago v0.5.0 (Ivic et al. (2024))
DE	Population-based	Indago v0.5.0 (Ivic et al. (2024))
MADS	Direct search	OMADS v2.1.0 (Bayoumy (2022))
NM	Direct search	scipy v1.11.4 (Virtanen et al. (2020))
L-BFGS-B	Gradient-based	scipy v1.11.4 (Virtanen et al. (2020))
BO	Model-based	Our implementation

The hyperparameters of all used algorithms (except BO and MADS) are set to their default recommended values by each Python module used, and can be found in each module’s documentation. All MADS hyperparameters are set as default (Bayoumy

(2022)) except for the scaling factor which is set to 10 as it is found to be a good value through numerical experimentation for all benchmarks. MADS, NM and LBFGSB are initialized using uniform random sampling.

Finally, the BO Python implementation is custom and it is based on the GP model with the Expected Improvement (EI) acquisition function (Zhan and Xing (2020)). The exploration hyperparameter of the EI is set to 0.01. The scikit-learn 1.2.2. (Pedregosa et al. (2011)) implementation of the GP model is utilized with the Matern kernel and the length scale parameter set to 1. The smoothness parameter ν is set to 2.5. This configuration was selected as it is one of the most popular default configurations used in Python BO modules such as scikit-optimize (Head et al. (2020)). Furthermore, in the GP model, the number of optimizer restarts is set to 2, and the target normalization feature is set to True. The L-BFGS-B optimizer with the Python module default parameters is used to find the maximum of EI in order to determine the best sample during each iteration (Virtanen et al. (2020)). The initial samples (initial sample size is 5 samples) of each BO run is generated using LHS to be as similar as possible to the ALPS framework, and the termination criterion is also set as the maximum number of allowed experimental model evaluations.

For a fair comparison with ALPS, we employ the custom BO implementation, avoiding the advanced model hyperparameter techniques often used in standard BO modules, usually with increased computational cost. These techniques could potentially enhance ALPS as well; however, our study aims to highlight the simplicity and effectiveness of our approach for inverse design. This approach performs well even when using out-of-the-box ML models with default hyperparameters.

Appendix C Inverse Design Convergence Results and Hyperparameter Analysis

In this section we present the complete results for all benchmarks and algorithms used for our numerical experiments, presented through both convergence graphs with uncertainty, and through solution reconstruction graphs. We also include a detailed analysis of the hyperparameters that are used in ALPS and how they affect its performance.

C.1 Synthetic Benchmarks Convergence

This section presents detailed convergence graphs and solution reconstruction graphs for the logistic growth and sinusoidal oscillation with damping benchmarks. Fig. C5 displays convergence graphs that include uncertainty metrics for both benchmarks across all algorithms. Fig. C6 and C7 illustrate the reconstructed solutions obtained by all optimization algorithms, compared with the target design. Tab. C3 and C4 provide comprehensive convergence statistics from 100 repeated runs for each optimization algorithm.

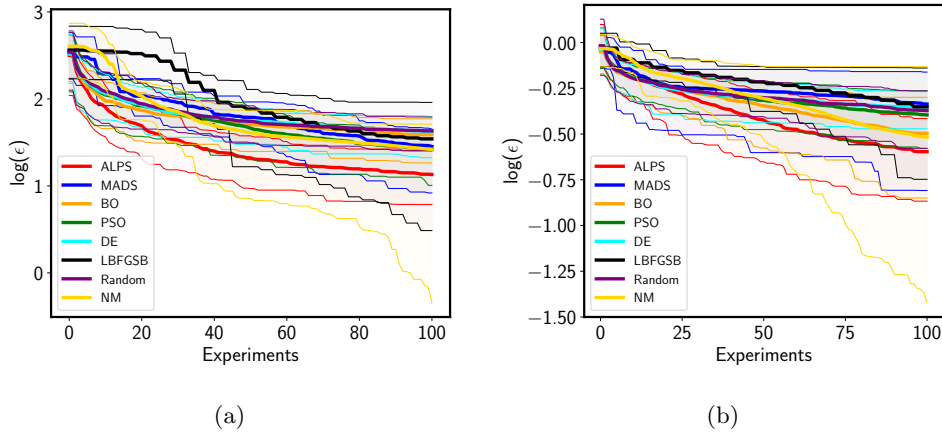
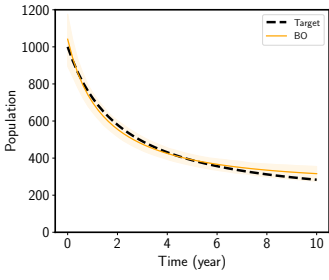
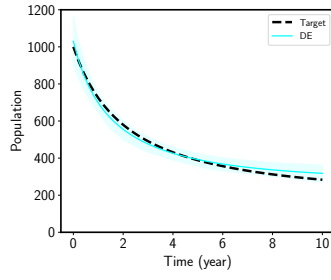


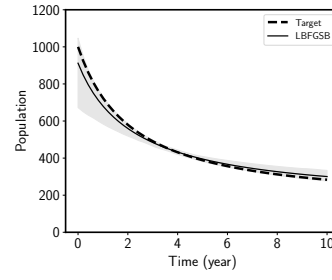
Fig. C5: Convergence graphs display the base-10 logarithm of the mean error value (Eq. (1)) for the synthetic benchmarks. The plots feature mean error values of 100 runs, represented by thick lines. Uncertainty bounds (shaded regions) are indicated by the 10th and 90th percentiles of the error across all algorithms: (a) Logistic growth target. (b) Sinusoidal oscillation with damping target.



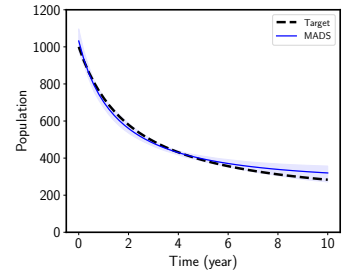
(a)



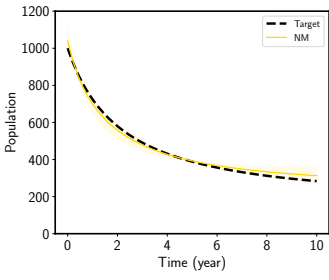
(b)



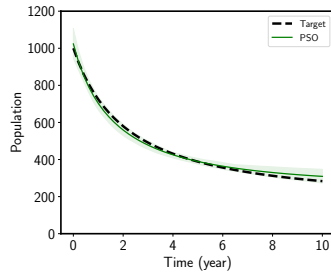
(c)



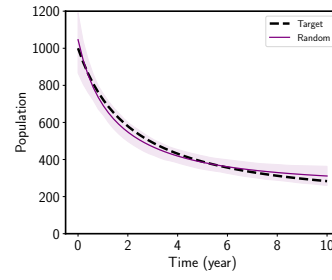
(d)



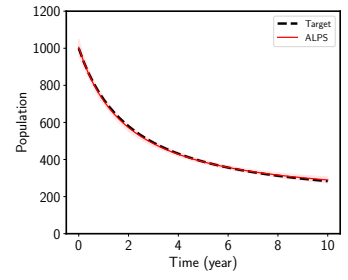
(e)



(f)



(g)



(h)

Fig. C6: The logistic growth solution reconstruction graphs of all optimization algorithms are presented: (a) BO algorithm. (b) DE algorithm. (c) LBFGSB algorithm. (d) MADS algorithm. (e) NM algorithm. (f) PSO algorithm. (g) Random sampling. (h) ALPS algorithm.

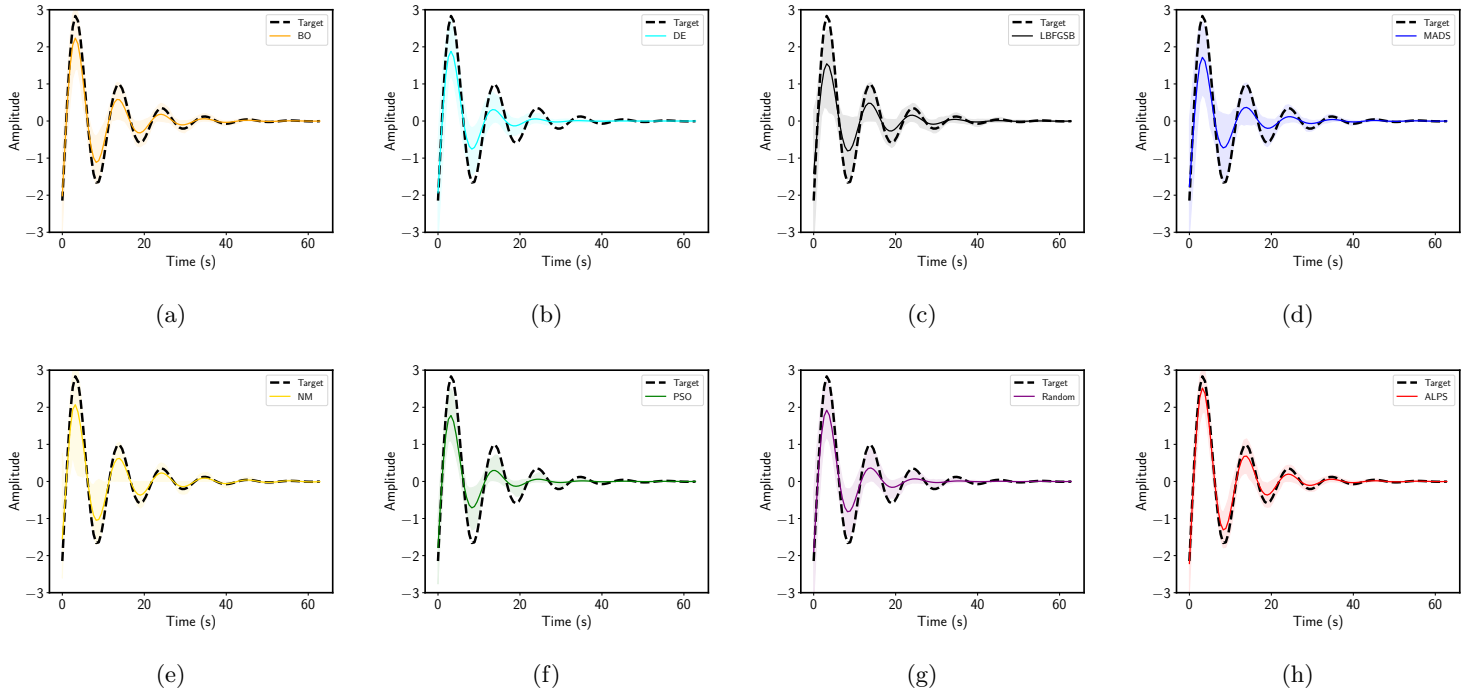


Fig. C7: The sinusoidal oscillation with damping solution reconstruction graphs of all optimization algorithms are presented: (a) BO algorithm. (b) DE algorithm. (c) LBFGSB algorithm. (d) MADS algorithm. (e) NM algorithm. (f) PSO algorithm. (g) Random sampling. (h) ALPS algorithm.

Table C3: Detailed convergence statistics of the ϵ value for the logistic growth benchmark, for all algorithms. The results are for 100 repeated runs. Smaller values are better.

Algorithm	Mean ϵ	Std ϵ	Maximum ϵ	Minimum ϵ
ALPS	13.52	9.030	67.08	2.91
MADS	28.40	14.00	57.93	1.50
BO	38.79	15.91	97.68	7.34
PSO	26.20	16.14	108.25	3.23
DE	41.77	16.38	112.56	4.72
LBFGB	34.70	34.83	114.52	0.22
Random	42.96	15.99	100.55	14.71
NM	26.30	28.95	131.88	0.10

Table C4: Detailed convergence statistics of the ϵ value for the sinusoidal oscillation with damping growth benchmark, for all algorithms. The results are for 100 repeated runs. Smaller values are better.

Algorithm	Mean ϵ	Std ϵ	Maximum ϵ	Minimum ϵ
ALPS	0.25	0.11	0.62	0.08
MADS	0.46	0.19	0.72	0.06
BO	0.31	0.13	0.63	0.07
PSO	0.40	0.11	0.60	0.10
DE	0.44	0.08	0.63	0.23
LBFGB	0.44	0.19	0.79	0.05
Random	0.42	0.10	0.62	0.16
NM	0.30	0.26	0.79	0.01

C.2 Photonic Surface Inverse Design Convergence

The detailed results of the photonic surface inverse design benchmarks are presented in this section. In Fig. C8, the convergence graphs with included uncertainty for all benchmarks and algorithms are shown. Fig. C9-C12 show the solution reconstruction graphs of all algorithms (except for ALPS) for the Inconel near-perfect emitter, Inconel TPV emitter, Stainless steel near-perfect emitter, and Stainless-steel TPV emitter, respectively. Finally, detailed convergence statistics are presented in Tab. C5-C8 following the same order as the solution reconstruction graphs.

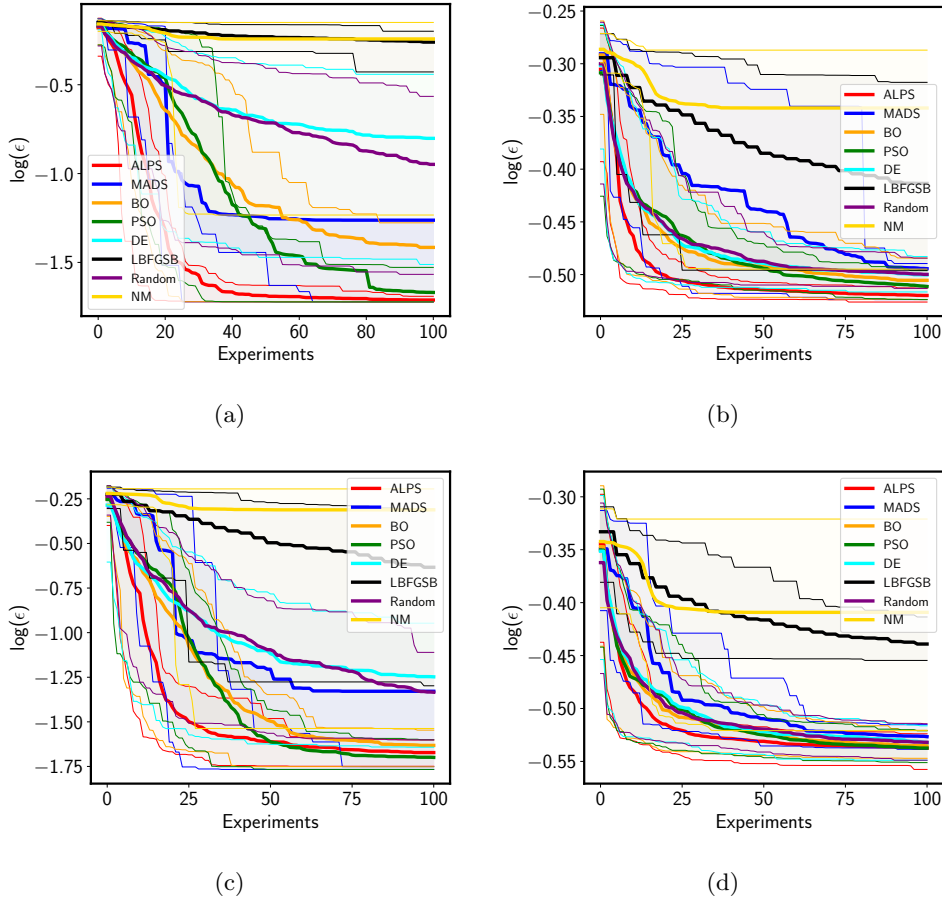


Fig. C8: Convergence graphs display the base-10 logarithm of the mean error value (Eq. (1)) for the photonic surface inverse design benchmarks, for all algorithms: (a) Inconel near-perfect emitter target. (b) Inconel TPV emitter target. (c) Stainless steel near-perfect emitter target. (d) Stainless steel TPV emitter target.

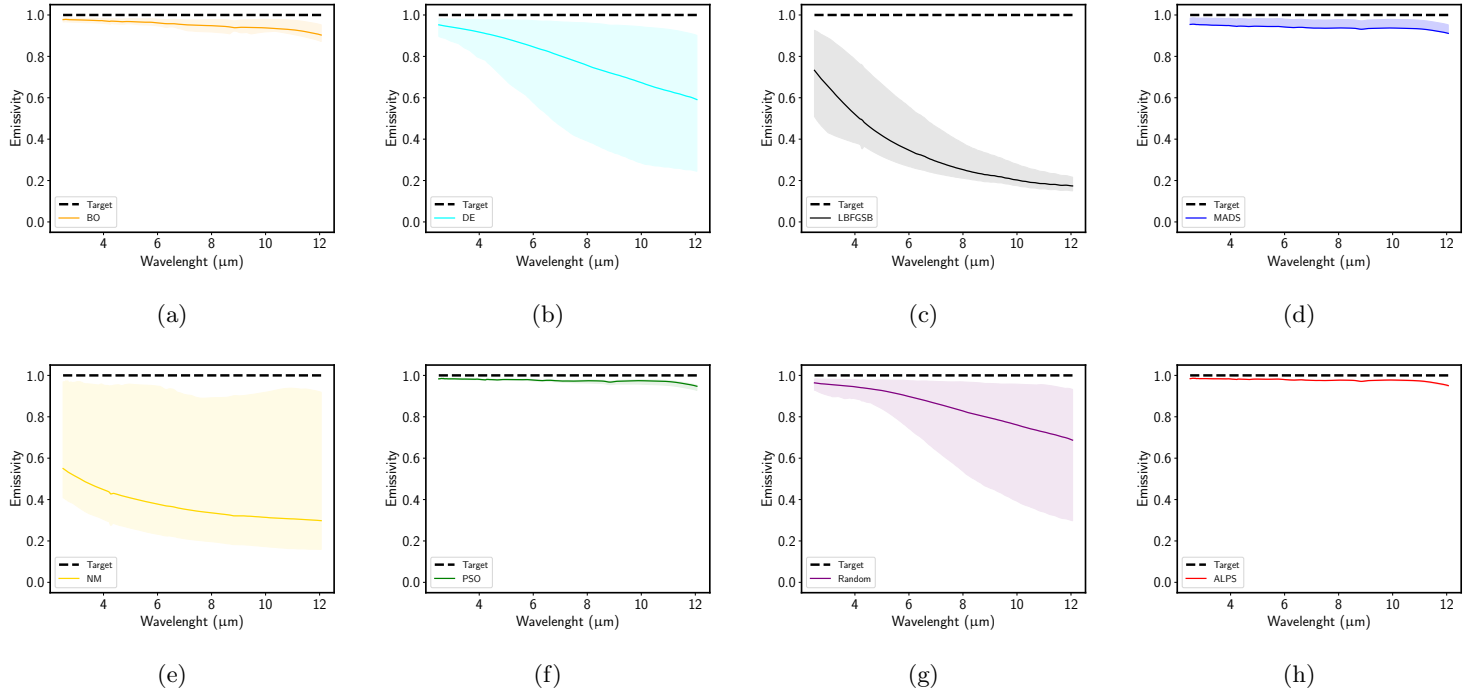


Fig. C9: The solution reconstruction graphs for the Inconel near-perfect emitter target for all optimization algorithms: (a) BO algorithm. (b) DE algorithm. (c) LBFGSB algorithm. (d) MADS algorithm. (e) NM algorithm. (f) PSO algorithm. (g) Random sampling. (h) ALPS algorithm.

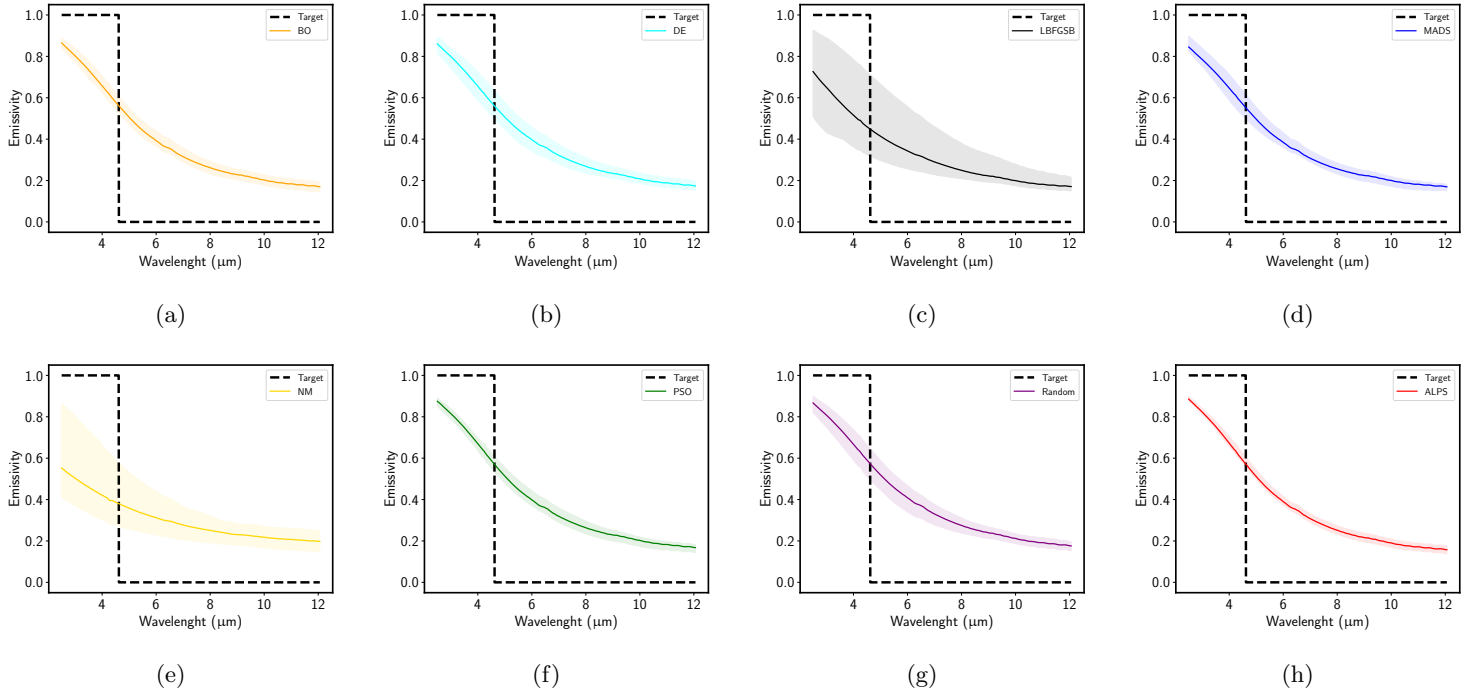


Fig. C10: The solution reconstruction graphs of the Inconel TPV emitter target for all optimization algorithms: (a) BO algorithm. (b) DE algorithm. (c) LBFGSB algorithm. (d) MADS algorithm. (e) NM algorithm. (f) PSO algorithm. (g) Random sampling. (h) ALPS algorithm.

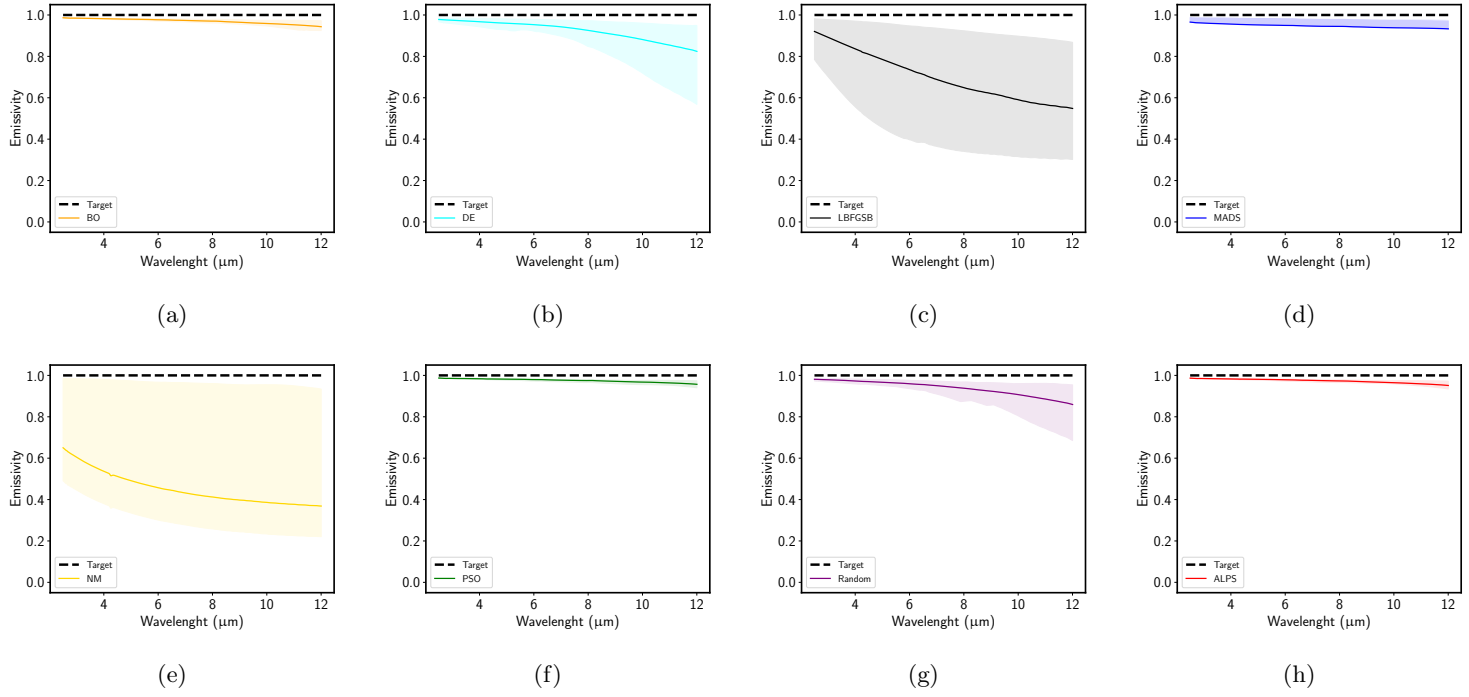


Fig. C11: The solution reconstruction graphs of the Stainless steel near-perfect emitter target for all optimization algorithms: (a) BO algorithm. (b) DE algorithm. (c) LBFGBS algorithm. (d) MADS algorithm. (e) NM algorithm. (f) PSO algorithm. (g) Random sampling. (h) ALPS algorithm.

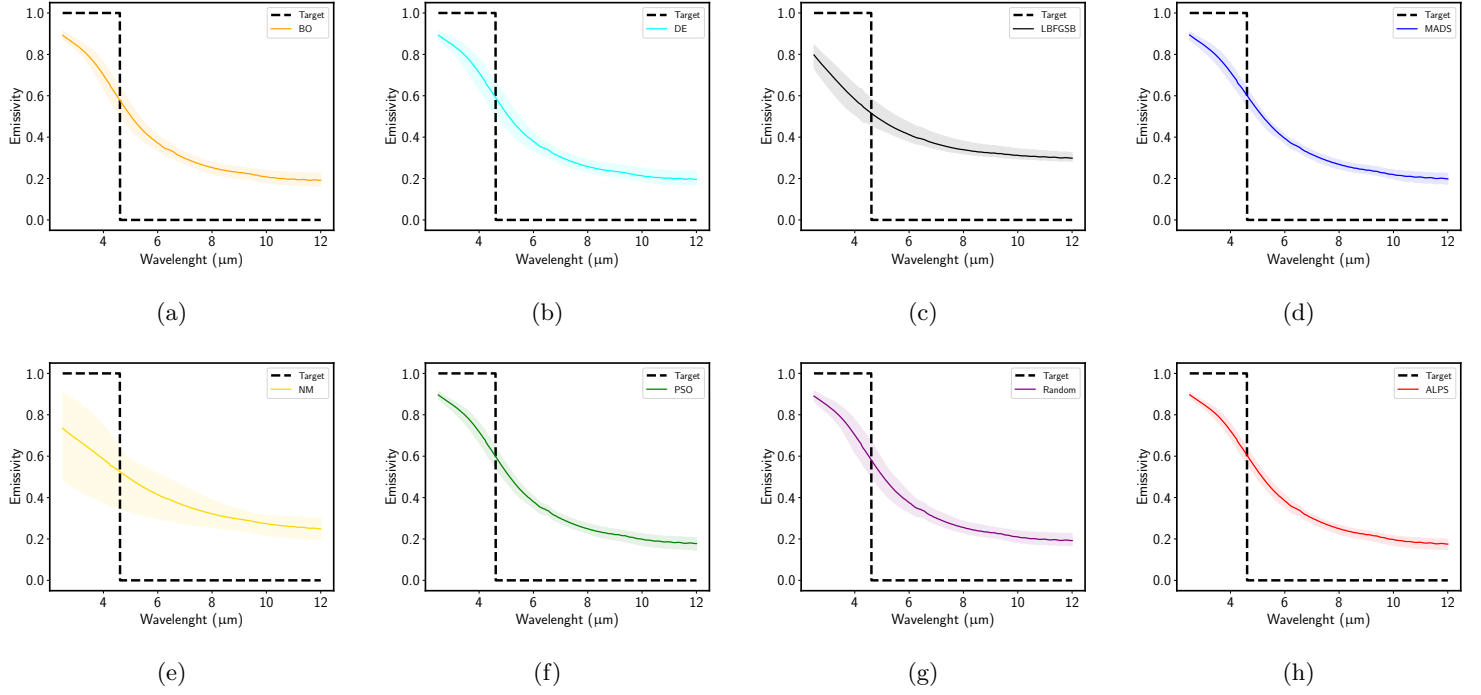


Fig. C12: The solution reconstruction graphs of the Stainless steel TPV emitter target for all optimization algorithms: (a) BO algorithm. (b) DE algorithm. (c) LBFGSB algorithm. (d) MADS algorithm. (e) NM algorithm. (f) PSO algorithm. (g) Random sampling. (h) ALPS algorithm.

Table C5: Detailed convergence statistics of the ϵ value for the Inconel near-perfect emitter target, for all algorithms. The results are for 100 repeated runs. Smaller values are better.

Algorithm	Mean ϵ	Std ϵ	Maximum ϵ	Minimum ϵ
ALPS	0.020	0.003	0.020	0.020
MADS	0.050	0.140	0.620	0.020
BO	0.040	0.050	0.390	0.020
PSO	0.020	0.010	0.050	0.020
DE	0.150	0.120	0.500	0.020
LBFGSB	0.550	0.080	0.690	0.370
Random	0.110	0.100	0.440	0.020
NM	0.570	0.220	0.730	0.020

Table C6: Detailed convergence statistics of the ϵ value for the Inconel TPV emitter target, for all algorithms. The results are for 100 repeated runs. Smaller values are better.

Algorithm	Mean ϵ	Std ϵ	Maximum ϵ	Minimum ϵ
ALPS	0.300	0.003	0.320	0.300
MADS	0.320	0.050	0.510	0.300
BO	0.310	0.020	0.400	0.300
PSO	0.310	0.010	0.340	0.300
DE	0.320	0.010	0.350	0.300
LBFGB	0.390	0.060	0.510	0.320
Random	0.320	0.010	0.340	0.300
NM	0.450	0.080	0.530	0.300

Table C7: Detailed convergence statistics of the ϵ value for the Stainless steel near-perfect emitter target, for all algorithms. The results are for 100 repeated runs. Smaller values are better.

Algorithm	Mean ϵ	Std ϵ	Maximum ϵ	Minimum ϵ
ALPS	0.021	0.003	0.042	0.017
MADS	0.057	0.145	0.632	0.017
BO	0.024	0.006	0.053	0.018
PSO	0.022	0.008	0.065	0.017
DE	0.056	0.040	0.247	0.022
LBFGB	0.194	0.171	0.530	0.035
Random	0.050	0.027	0.133	0.019
NM	0.482	0.220	0.650	0.018

Table C8: Detailed convergence statistics of the ϵ value for the Stainless steel TPV emitter target, for all algorithms. The results are for 100 repeated runs. Smaller values are better.

Algorithm	Mean ϵ	Std ϵ	Maximum ϵ	Minimum ϵ
ALPS	0.290	0.010	0.300	0.280
MADS	0.300	0.070	0.320	0.280
BO	0.290	0.010	0.310	0.280
PSO	0.290	0.010	0.320	0.280
DE	0.290	0.010	0.320	0.280
LBFGB	0.360	0.020	0.440	0.350
Random	0.290	0.010	0.330	0.280
NM	0.390	0.070	0.600	0.280

C.3 ALPS Hyperparameter Analysis

In this section we present the analysis of how ALPS and the RF algorithm hyperparameters affect its performance. We separately analyze the RF hyperparameters and the ALPS hyperparameters on four different benchmarks (two synthetic benchmarks, and two photonic surface inverse design benchmarks, namely Inconel near-perfect emitter target, and the Stainless steel TPV emitter target). Each ALPS run is repeated 100 times for all benchmarks to account the stochasticity in the algorithm.

C.3.1 Influence of RF Hyperparameters

Firstly, in order to study the influence of the RF algorithm, we consider changing only two parameters, namely the number of estimators (or trees) and the maximum tree depth value. We further investigate these two hyperparameters because they are the only ones that differ from the default settings in scikit-learn 1.2.2 in our experimental model (see App. A.3), which was optimized in our previous work (Grbic et al. (2024)). The ALPS hyperparameters used during the RF algorithm are the same as the ones presented in Sec. 3, i.e., initial sample size and batch size are both set to 5, and the surrogate sample size is set to 600.

In Fig. C13, the results of the RF algorithm used in ALPS are presented for the four different benchmarks. The number of estimators considered for this analysis is set to 150, 250, and 450, while the varied maximum depth values are 3, 5, and 10. It can be observed that changing the hyperparameters of the RF algorithm within ALPS does not affect the performance of ALPS with the exception the logistic growth benchmark case (Tab. C9). This means that using the default out-of-the-box parameters of the RF algorithm (in scikit-learn v1.2.2.) are suitable when we want to apply it within ALPS. This is beneficial as it shows the robustness of the approach, however, it also implies that there is not a lot of room for improvement of the approach that can be achieved by tuning the RF hyperparameters. Detailed convergence statistics for all benchmarks and all RF hyperparameter combinations are given in Tab. C9-C12.

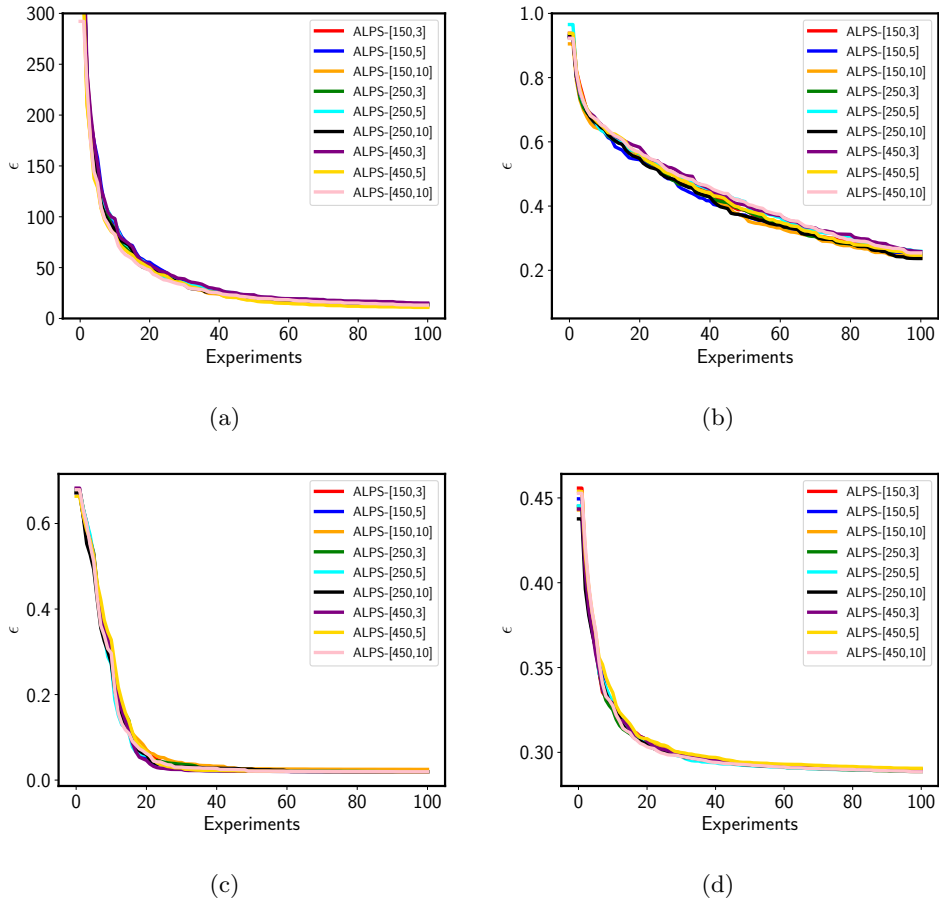


Fig. C13: Convergence graphs for all investigated RF algorithm hyperparameters and a selection of benchmarks, the first number in each bracket represents the number of estimators (trees), while the second number is the maximum depth value: (a) Logistic growth benchmark. (b) Sinusoidal oscillation with damping benchmark. (c) Photonic surface benchmark: Inconel near-perfect emitter target. (d) Photonic surface benchmark: Stainless steel TPV emitter target.

Table C9: Detailed convergence statistics of the ϵ value for the logistic growth benchmark, for all investigated RF hyperparameter values. Results are for 100 repeated runs.

Estimators	Max depth	Mean ϵ	Std ϵ
150	3	14.37	11.97
150	5	14.18	17.40
150	10	11.45	6.66
250	3	13.40	11.37
250	5	13.95	13.12
250	10	13.29	11.70
450	3	15.14	13.40
450	5	10.88	7.16
450	10	13.13	8.29

Table C10: Detailed convergence statistics of the ϵ value for the sinusoidal oscillation with damping benchmark, for all investigated RF hyperparameter values. Results are for 100 repeated runs.

Estimators	Max depth	Mean ϵ	Std ϵ
150	3	0.25	0.12
150	5	0.25	0.12
150	10	0.24	0.10
250	3	0.25	0.12
250	5	0.26	0.12
250	10	0.24	0.10
450	3	0.26	0.12
450	5	0.25	0.11
450	10	0.25	0.11

Table C11: Detailed convergence statistics of the ϵ value for the photonic surface benchmark–Inconel near-perfect emitter target, for all investigated RF hyperparameter values. Results are for 100 repeated runs.

Estimators	Max depth	Mean ϵ	Std ϵ
150	3	0.020	0.020
150	5	0.020	0.020
150	10	0.025	0.060
250	3	0.020	0.020
250	5	0.020	0.020
250	10	0.020	0.020
450	3	0.020	0.020
450	5	0.020	0.020
450	10	0.020	0.020

Table C12: Detailed convergence statistics of the ϵ value for the photonic surface benchmark–Stainless steel TPV emitter target, for all investigated RF hyperparameter values. Results are for 100 repeated runs.

Estimators	Max depth	Mean ϵ	Std ϵ
150	3	0.290	0.010
150	5	0.290	0.010
150	10	0.290	0.010
250	3	0.290	0.010
250	5	0.290	0.010
250	10	0.290	0.010
450	3	0.290	0.010
450	5	0.290	0.010
450	10	0.290	0.010

C.3.2 Influence of ALPS Hyperparameters

In this section we show the results of how ALPS hyperparameters influence its performance. For our initial comparison with other optimization algorithms, we use the initial sample size, and batch size both set to 5, and the surrogate sample size set to 600. We keep the same initial size, however, we vary the batch size as 1, 5, 10, and 20, and we set the surrogate sample size as either 300, 600 or 1200. We repeat every run 100 times and obtain the convergence graphs for each ALPS hyperparameter variant. Fig. C14 shows the convergence graphs of all ALPS investigated hyperparameters, for all four benchmarks. ALPS hyperparameters have a larger impact on the synthetic benchmarks (Fig. C14a-C14b) than on the photonic surface inverse design benchmarks (Fig. C14c-C14d). Detailed convergence statistics for all benchmarks are given in Tab. C13-C16.

Increasing the surrogate sample size has an impact on the logistic growth benchmark (Tab C13). For both synthetic benchmarks, using smaller batch sizes (sequential sampling) enhances the performance of ALPS in terms of the mean ϵ , even more so on the sinusoidal oscillation with damping benchmark (Tab C14). Utilizing the worst performing hyperparameter set ($n_{batch}=20$, $n_s=300$) on the logistic growth benchmark yields better results in the mean ϵ (19.79), than PSO, which is the second best performing optimization algorithm, that yields the mean of ϵ of 26.20 (Tab. C3). For the sinusoidal oscillation with damping benchmark, the worst performing hyperparameter set is the same, and it would rank as the third best if compared to the other investigated optimization algorithms (Tab. C4).

For the main problem of photonic surface inverse design, the influence of ALPS hyperparameters is not as pronounced. In Fig. C14c, the convergence graph for the Inconel near-perfect emitter target is shown. In terms of the final mean value of ϵ , there is not a large difference, with the exception of the case when n_{batch} is 1, and the n_s values are either 600 or 1200, the final mean of ϵ is higher compared to other hyperparameter sets (Tab. C15). Both of these hyperparameter sets had exactly one run out of 100, where ALPS converged to a local optimum and obtained a maximum final ϵ value of 0.68 and 0.61 for $n_s=600$, and $n_s=1200$, respectively. For the Stainless steel TPV emitter target, all ALPS hyperparameter variants perform the same as presented in Tab. C16). The main benefit of using a smaller value of n_{batch} can be observed in Fig. C14c for the Inconel near-perfect emitter, where lower values have a tendency of converging to a satisfying design shortly after 20 experimental model evaluations, while a larger value delays this for additional experimental model evaluations. This performance is not apparent for the Stainless steel TPV emitter (Fig. C14d).

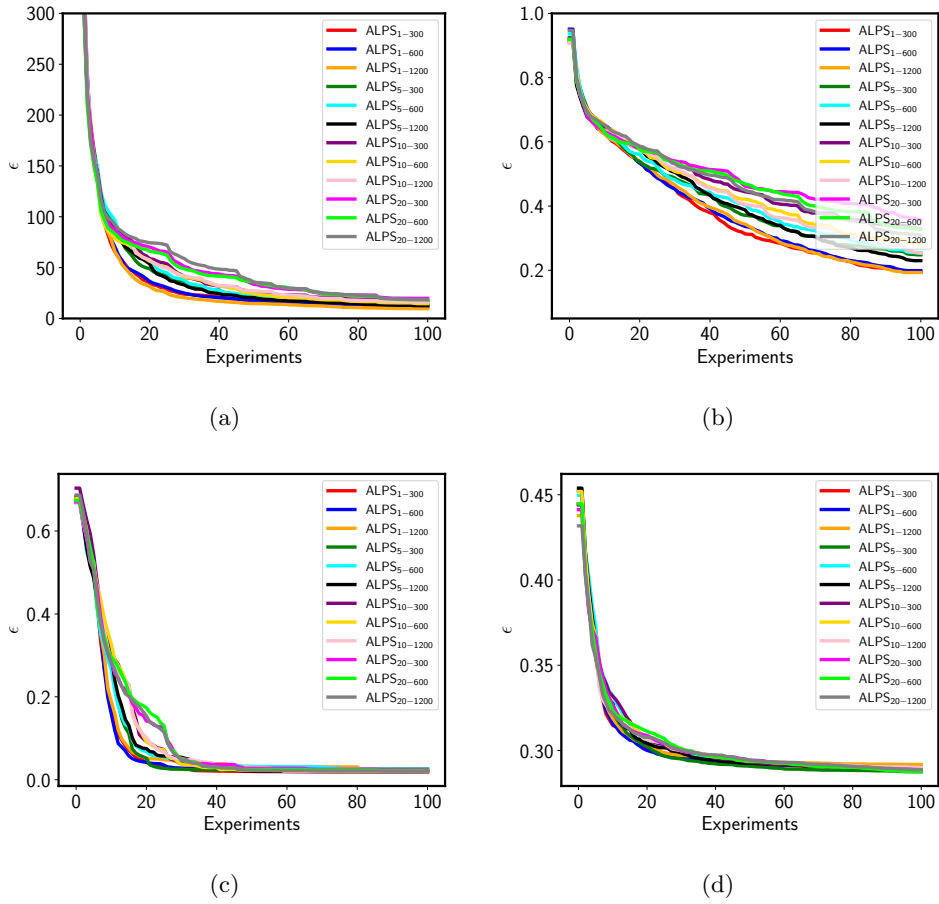


Fig. C14: Convergence graphs for all investigated ALPS hyperparameters and a selection of benchmarks, the first number in the index represents the batch size, while the second number is the surrogate sample size: (a) Logistic growth benchmark. (b) Sinusoidal oscillation with damping benchmark. (c) Photonic surface benchmark: Inconel near-perfect emitter target. (d) Photonic surface benchmark: Stainless steel TPV emitter target.

Table C13: Detailed convergence statistics of the ϵ value for the logistic growth benchmark, for all investigated ALPS hyperparameter values. Results are for 100 repeated runs.

nbatch	n_s	Mean ϵ	Std ϵ
1	300	11.50	12.15
1	600	12.58	13.40
1	1200	9.67	10.51
5	300	14.10	7.42
5	600	13.43	9.68
5	1200	12.56	12.25
10	300	16.75	9.64
10	600	14.57	10.33
10	1200	16.02	13.62
20	300	19.79	8.21
20	600	18.40	10.44
20	1200	18.33	11.96

Table C14: Detailed convergence statistics of the ϵ value for the sinusoidal oscillation with damping benchmark, for all investigated ALPS hyperparameter values. Results are for 100 repeated runs.

n_{batch}	n_s	Mean ϵ	Std ϵ
1	300	0.19	0.10
1	600	0.20	0.12
1	1200	0.19	0.14
5	300	0.25	0.10
5	600	0.25	0.12
5	1200	0.23	0.11
10	300	0.33	0.12
10	600	0.28	0.12
10	1200	0.25	0.13
20	300	0.36	0.12
20	600	0.33	0.12
20	1200	0.31	0.14

Table C15: Detailed convergence statistics of the ϵ value for the photonic surface benchmark–Inconel near-perfect emitter target, for all investigated ALPS hyperparameter values. Results are for 100 repeated runs.

n_{batch}	n_s	Mean ϵ	Std ϵ
1	300	0.020	0.001
1	600	0.030	0.070
1	1200	0.030	0.060
5	300	0.020	0.001
5	600	0.020	0.001
5	1200	0.020	0.001
10	300	0.020	0.001
10	600	0.020	0.001
10	1200	0.020	0.001
20	300	0.020	0.001
20	600	0.020	0.001
20	1200	0.020	0.001

Table C16: Detailed convergence statistics of the ϵ value for the photonic surface benchmark–Stainless steel TPV emitter target, for all investigated ALPS hyperparameter values. Results are for 100 repeated runs.

n_{batch}	n_s	Mean ϵ	Std ϵ
1	300	0.290	0.010
1	600	0.290	0.010
1	1200	0.290	0.010
5	300	0.290	0.010
5	600	0.290	0.010
5	1200	0.290	0.010
10	300	0.290	0.010
10	600	0.290	0.010
10	1200	0.290	0.010
20	300	0.290	0.010
20	600	0.290	0.010
20	1200	0.290	0.010

C.4 ALPS with Warm Starting Inverse Design Convergence

In this section the ALPS convergence results with and without warm starting are presented. The convergence details for the cross-target warm starting cases are presented in Tab. C17-C20, while Tab. C21-C24 show the results of the cross-material warm starting cases.

Table C17: Detailed convergence statistics of the ϵ value for ALPS with and without cross-target warm starting. The target is the Inconel near-perfect emitter warm started by a prior inverse design model for an Inconel TPV emitter. The results are for 100 repeated runs.

Algorithm	Mean ϵ	Std ϵ	Maximum ϵ	Minimum ϵ
ALPS _{<i>ws=True</i>}	0.020	0.001	0.020	0.020
ALPS _{<i>ws=False</i>}	0.020	0.001	0.020	0.020

Table C18: Detailed convergence statistics of the ϵ value for ALPS with and without cross-target warm starting. The target is the Inconel TPV emitter warm started by a prior inverse design model for an Inconel near-perfect emitter. The results are for 100 repeated runs.

Algorithm	Mean ϵ	Std ϵ	Maximum ϵ	Minimum ϵ
ALPS _{<i>ws=True</i>}	0.300	0.001	0.310	0.300
ALPS _{<i>ws=False</i>}	0.300	0.001	0.310	0.300

Table C19: Detailed convergence statistics of the ϵ value for ALPS with and without cross-target warm starting. The target is the Stainless steel near-perfect emitter warm started by a prior inverse design model for a Stainless steel TPV emitter. The results are for 100 repeated runs.

Algorithm	Mean ϵ	Std ϵ	Maximum ϵ	Minimum ϵ
ALPS _{<i>ws=True</i>}	0.020	0.001	0.040	0.020
ALPS _{<i>ws=False</i>}	0.020	0.001	0.040	<i>mathbf{0.020}</i>

Table C20: Detailed convergence statistics of the ϵ value for ALPS with and without cross-target warm starting. The target is the Stainless steel TPV emitter warm started by a prior inverse design model for a Stainless steel near-perfect emitter. The results are for 100 repeated runs.

Algorithm	Mean ϵ	Std ϵ	Maximum ϵ	Minimum ϵ
ALPS _{<i>ws=True</i>}	0.290	0.010	0.300	0.280
ALPS _{<i>ws=False</i>}	0.290	0.010	0.310	0.280

Table C21: Detailed convergence statistics of the ϵ value for ALPS with and without cross-material warm starting. The target is the Inconel near-perfect emitter warm started by a prior inverse design model for an Stainless steel TPV emitter. The results are for 100 repeated runs.

Algorithm	Mean ϵ	Std ϵ	Maximum ϵ	Minimum ϵ
ALPS _{<i>ws=True</i>}	0.020	0.001	0.020	0.020
ALPS _{<i>ws=False</i>}	0.020	0.001	0.020	0.020

Table C22: Detailed convergence statistics of the ϵ value for ALPS with and without cross-material warm starting. The target is the Inconel TPV emitter warm started by a prior inverse design model for an Stainless steel near-perfect emitter. The results are for 100 repeated runs.

Algorithm	Mean ϵ	Std ϵ	Maximum ϵ	Minimum ϵ
ALPS _{<i>ws=True</i>}	0.300	0.010	0.310	0.280
ALPS _{<i>ws=False</i>}	0.290	0.010	0.300	0.280

Table C23: Detailed convergence statistics of the ϵ value for ALPS with and without cross-material warm starting. The target is the Stainless steel near-perfect emitter warm started by a prior inverse design model for a Inconel TPV emitter. The results are for 100 repeated runs.

Algorithm	Mean ϵ	Std ϵ	Maximum ϵ	Minimum ϵ
ALPS _{<i>ws=True</i>}	0.020	0.001	0.040	0.020
ALPS _{<i>ws=False</i>}	0.020	00.001	0.040	0.020

Table C24: Detailed convergence statistics of the ϵ value for ALPS with and without cross-material warm starting. The target is the Stainless steel TPV emitter warm started by a prior inverse design model for a Inconel near-perfect emitter. The results are for 100 repeated runs.

Algorithm	Mean ϵ	Std ϵ	Maximum ϵ	Minimum ϵ
ALPS _{<i>ws=True</i>}	0.300	0.001	0.310	0.300
ALPS _{<i>ws=False</i>}	0.300	0.001	0.320	0.300

References

- Brewster MQ. Thermal radiative transfer and properties. John Wiley & Sons; 1992.
- Howell JR, Mengüç MP, Daun K, Siegel R. Thermal radiation heat transfer. CRC press; 2020.
- Fan D, Burger T, McSherry S, Lee B, Lenert A, Forrest SR. Near-perfect photon utilization in an air-bridge thermophotovoltaic cell. *Nature*. 2020;586(7828):237–241.
- LaPotin A, Schulte KL, Steiner MA, Buznitsky K, Kelsall CC, Friedman DJ, et al. Thermophotovoltaic efficiency of 40%. *Nature*. 2022;604(7905):287–291.
- Raman AP, Anoma MA, Zhu L, Rephaeli E, Fan S. Passive radiative cooling below ambient air temperature under direct sunlight. *Nature*. 2014;515(7528):540–544.
- Heo SY, Lee GJ, Kim DH, Kim YJ, Ishii S, Kim MS, et al. A Janus emitter for passive heat release from enclosures. *Science advances*. 2020;6(36):eabb1906.
- Menon AK, Haechler I, Kaur S, Lubner S, Prasher RS. Enhanced solar evaporation using a photo-thermal umbrella for wastewater management. *Nature Sustainability*. 2020;3(2):144–151.
- Ni G, Li G, Boriskina SV, Li H, Yang W, Zhang T, et al. Steam generation under one sun enabled by a floating structure with thermal concentration. *Nature Energy*. 2016;1(9):1–7.
- Weinstein LA, Loomis J, Bhatia B, Bierman DM, Wang EN, Chen G. Concentrating solar power. *Chemical reviews*. 2015;115(23):12797–12838.
- He YL, Qiu Y, Wang K, Yuan F, Wang WQ, Li MJ, et al. Perspective of concentrating solar power. *Energy*. 2020;198:117373.
- Wiecha PR, Arbouet A, Girard C, Muskens OL. Deep learning in nano-photonics: inverse design and beyond. *Photonics Research*. 2021;9(5):B182–B200.
- Ma W, Liu Z, Kudyshev ZA, Boltasseva A, Cai W, Liu Y. Deep learning for the design of photonic structures. *Nature Photonics*. 2021;15(2):77–90.
- Mao S, Cheng L, Zhao C, Khan FN, Li Q, Fu H. Inverse design for silicon photonics: from iterative optimization algorithms to deep neural networks. *Applied Sciences*. 2021;11(9):3822.
- Wang N, Yan W, Qu Y, Ma S, Li SZ, Qiu M. Intelligent designs in nanophotonics: from optimization towards inverse creation. *PhotoniX*. 2021;2:1–35.

- Xu X, Sun C, Li Y, Zhao J, Han J, Huang W. An improved tandem neural network for the inverse design of nanophotonics devices. *Optics Communications*. 2021;481:126513.
- Park M, Grbčić L, Motameni P, Song S, Singh A, Malagrino D, et al. Inverse Design of Photonic Surfaces via High throughput Femtosecond Laser Processing and Tandem Neural Networks. *Advanced Science*. 2024;p. 2401951.
- Ma T, Tobah M, Wang H, Guo LJ. Benchmarking deep learning-based models on nanophotonic inverse design problems. *Opto-Electronic Science*. 2022;1(1):210012–1.
- Jiang J, Fan JA. Simulator-based training of generative neural networks for the inverse design of metasurfaces. *Nanophotonics*. 2020;9(5):1059–1069.
- Kudyshev ZA, Kildishev AV, Shalaev VM, Boltasseva A. Machine-learning-assisted metasurface design for high-efficiency thermal emitter optimization. *Applied Physics Reviews*. 2020;7(2).
- Liu Z, Zhu Z, Cai W. Topological encoding method for data-driven photonics inverse design. *Optics express*. 2020;28(4):4825–4835.
- Liu Z, Zhu D, Raju L, Cai W. Tackling photonic inverse design with machine learning. *Advanced Science*. 2021;8(5):2002923.
- Habibi M, Wang J, Fuge M. When Is it Actually Worth Learning Inverse Design? In: *International Design Engineering Technical Conferences and Computers and Information in Engineering Conference*. vol. 87301. American Society of Mechanical Engineers; 2023. p. V03AT03A025.
- Zhu Y, Chen Y, Gorsky S, Shubitidze T, Dal Negro L. Inverse design of functional photonic patches by adjoint optimization coupled to the generalized Mie theory. *JOSA B*. 2023;40(7):1857–1874.
- Gershnel E, Chen M, Mao C, Wang EW, Lalanne P, Fan JA. Reparameterization Approach to Gradient-Based Inverse Design of Three-Dimensional Nanophotonic Devices. *ACS Photonics*. 2022;10(4):815–823.
- Hughes TW, Minkov M, Williamson IA, Fan S. Adjoint method and inverse design for nonlinear nanophotonic devices. *ACS Photonics*. 2018;5(12):4781–4787.
- Minkov M, Williamson IA, Andreani LC, Gerace D, Lou B, Song AY, et al. Inverse design of photonic crystals through automatic differentiation. *Acs Photonics*. 2020;7(7):1729–1741.
- Lalau-Keraly CM, Bhargava S, Miller OD, Yablonovitch E. Adjoint shape optimization applied to electromagnetic design. *Optics express*. 2013;21(18):21693–21701.

- Wang K, Ren X, Chang W, Lu L, Liu D, Zhang M. Inverse design of digital nanophotonic devices using the adjoint method. *Photonics Research*. 2020;8(4):528–533.
- Molesky S, Lin Z, Piggott AY, Jin W, Vucković J, Rodriguez AW. Inverse design in nanophotonics. *Nature Photonics*. 2018;12(11):659–670.
- Deng L, Xu Y, Liu Y. Hybrid inverse design of photonic structures by combining optimization methods with neural networks. *Photonics and Nanostructures-Fundamentals and Applications*. 2022;52:101073.
- Kudyshev ZA, Kildishev AV, Shalaev VM, Boltasseva A. Machine learning-assisted global optimization of photonic devices. *Nanophotonics*. 2020;10(1):371–383.
- Hegde RS. Photonics inverse design: pairing deep neural networks with evolutionary algorithms. *IEEE Journal of Selected Topics in Quantum Electronics*. 2019;26(1):1–8.
- Yao T, Huang T, Yan B, Ge M, Yin J, Peng C, et al. Inverse design of dispersion for photonic devices based on LSTM and gradient-free optimization algorithms hybridization. *JOSA B*. 2023;40(6):1525–1532.
- Kudyshev ZA, Kildishev AV, Shalaev VM, Boltasseva A. Optimizing startshot lightsail design: A generative network-based approach. *ACS Photonics*. 2021;9(1):190–196.
- Yeung C, Pham B, Tsai R, Fountaine KT, Raman AP. DeepAdjoint: an all-in-one photonic inverse design framework integrating data-driven machine learning with optimization algorithms. *ACS Photonics*. 2022;10(4):884–891.
- Yeung C, Ho D, Pham B, Fountaine KT, Zhang Z, Levy K, et al. Enhancing adjoint optimization-based photonic inverse design with explainable machine learning. *ACS Photonics*. 2022;9(5):1577–1585.
- Grbcic L, Park M, Elzouka M, Prasher R, Müller J, Grigoropoulos CP, et al.: Inverse design of photonic surfaces on Inconel via multi-fidelity machine learning ensemble framework and high throughput femtosecond laser processing.
- Noack M, Ushizima D. *Methods and Applications of Autonomous Experimentation*. CRC Press (Unlimited); 2023.
- Häse F, Roch LM, Aspuru-Guzik A. Next-generation experimentation with self-driving laboratories. *Trends in Chemistry*. 2019;1(3):282–291.
- Kochenderfer MJ, Wheeler TA. *Algorithms for optimization*. Mit Press; 2019.
- Paria B, Póczos B, Ravikumar P, Schneider J, Suggala AS. Be greedy—a simple algorithm for blackbox optimization using neural networks. In: *ICML2022 Workshop on Adaptive Experimental Design and Active Learning in the Real World*; 2022. .

- Wang C, Duan Q, Gong W, Ye A, Di Z, Miao C. An evaluation of adaptive surrogate modeling based optimization with two benchmark problems. *Environmental Modelling & Software*. 2014;60:167–179.
- Elzouka M, Yang C, Albert A, Prasher RS, Lubner SD. Interpretable forward and inverse design of particle spectral emissivity using common machine-learning models. *Cell Reports Physical Science*. 2020;1(12).
- Liu H, Cai J, Ong YS. Remarks on multi-output Gaussian process regression. *Knowledge-Based Systems*. 2018;144:102–121.
- Pedregosa F, Varoquaux G, Gramfort A, Michel V, Thirion B, Grisel O, et al. Scikit-learn: Machine learning in Python. *the Journal of machine Learning research*. 2011;12:2825–2830.
- Jones DR. A taxonomy of global optimization methods based on response surfaces. *Journal of global optimization*. 2001;21:345–383.
- Breiman L. Random forests. *Machine learning*. 2001;45:5–32.
- Kennedy J, Eberhart R. Particle swarm optimization. In: *Proceedings of ICNN'95-international conference on neural networks*. vol. 4. ieee; 1995. p. 1942–1948.
- Storn R, Price K. Differential evolution—a simple and efficient heuristic for global optimization over continuous spaces. *Journal of global optimization*. 1997;11:341–359.
- Audet C, Dennis Jr JE. Mesh adaptive direct search algorithms for constrained optimization. *SIAM Journal on optimization*. 2006;17(1):188–217.
- Lagarias JC, Reeds JA, Wright MH, Wright PE. Convergence properties of the Nelder–Mead simplex method in low dimensions. *SIAM Journal on optimization*. 1998;9(1):112–147.
- Shahriari B, Swersky K, Wang Z, Adams RP, De Freitas N. Taking the human out of the loop: A review of Bayesian optimization. *Proceedings of the IEEE*. 2015;104(1):148–175.
- Ivic S, Druzeta S, Grbic L.: Indago v0.5.0. PyPI. Available from: <https://pypi.org/project/Indago/>.
- Bayoumy A.: OMADS. Github. Available from: <https://github.com/Ahmed-Bayoumy/OMADS>.
- Virtanen P, Gommers R, Oliphant TE, Haberland M, Reddy T, Cournapeau D, et al. SciPy 1.0: fundamental algorithms for scientific computing in Python. *Nature methods*. 2020;17(3):261–272.

Zhan D, Xing H. Expected improvement for expensive optimization: a review. *Journal of Global Optimization*. 2020;78(3):507–544.

Head T, Kumar M, Nahrstaedt H, Louppe G, Shcherbatyi I.: scikit-optimize/scikit-optimize. Zenodo. Available from: <https://doi.org/10.5281/zenodo.4014775>.